A synergistic vortex generator for improved wake effects in piezoelectric fluid energy harvesters: a numerical study

Runze Zhang, Yu Cong, Mohammed Sellam, Amer Chpoun, Shuitao Gu

A synergistic vortex generator for improved wake effects in piezoelectric fluid energy harvesters: a numerical study

R. Z. Zhang [a], **Y. Cong** [a], **M. Sellam** [a], **A. Chpoun** [a]. **S. T. Gu** [b].

[a] *Université Paris-Saclay, Univ Evry, LMEE, 91020, Evry, France*

[b] *School of Civil Engineering, Chongqing University, Chongqing 400044, China*

Abstract

A synergistic vortex generator, composed of upstream double plates and a downstream cylinder with small spacing, is investigated through numerical simulations to enhance wake effects and, subsequently, the power output of a piezoelectric energy harvesting system in a flowing water environment. The simulations illustrate the synergistic mechanisms, demonstrating that adjusting the angle of the double plates allows the synergistic vortex generator to produce distinct wake patterns compared to the configurations with double plates or a cylinder alone, significantly impacting the dynamic behavior and power output of the harvester. Notably, when the double plate angles are set at $-15°$ and $30°$, the asymmetric double-plate wake type generates high-frequency, large-amplitude vibrations in the flexible piezoelectric flag, resulting in stable power output, which cannot be achieved by classical cylinder-based and double-plate-based harvesters. In particular, at the angle of $-15°$, the synergistic harvester exhibits a 190% increase in amplitude, a 127% increase in vibration frequency, a 1000% increase in power output, and a 280% improvement in energy harvesting efficiency compared to cylinder-based harvesters. At larger double-plate angles ($-90°$ to $-45°$ and $60°$ to $90°$), the reduced blockage from the plates weakens the vortex strength they generate, leaving the flexible piezoelectric flag predominantly influenced by the vortices shed from the cylinder. However, the flag's vibrations remain significantly enhanced compared to cylinder-based systems due to the merging of wakes from both the double plates and the cylinder. Overall, the larger the angle of the plates, the weaker the synergistic enhancement effect. Additionally, different angles lead to varying wake center velocity profiles, with the centerline velocity of the double-plate wake type generally lower than that of the cylinder wake type. Thus, future optimizations of energy harvester arrays could benefit from adjusting the plate angles to maximize collective power output.

Keywords: Fluid-structure-piezoelectric coupling; Vortex generator; Wake induced vibration; Piezoelectric fluid energy harvester.

1 Introduction

With the advancement of wireless sensor networks or sensor nodes [1], the demand for micro-electronic devices in remote areas is also gradually increasing. To address the power supply issues for these devices, self-powered piezoelectric fluid energy harvesters (PFEH) have gained much attention. These harvesters are ideal for the replacements of traditional chemistry batteries [2] with limited lifespan due to their simple structure, high energy conversion efficiency, and the ability to continuously generate power from the kinetic energy of renewable energy source, i.e. flowing fluid environments without the need for supervision. The general mechanisms of PFEH include flutter [3, 4], vortex-induced vibration (VIV) [5, 6], and galloping [7, 8]. Typically a single vortex generator will be used for harvesting energy. Although their principles of flow induce vibration are already well understood, their effectiveness in enhancing power output is limited. Currently, research on wake induced vibration (WIV) energy harvesters using multiple vortex generators is becoming popular [9]. The complex vortex interactions between different vortex generators will significantly enhance the performance of these harvesters.

When a PFEH consists only of a flexible piezoelectric laminated flag immersed in dynamic fluid, coupled with a electric circuit containing resistive loads and electrodes, its energy harvesting primarily relies on flutter induced by structural and fluid nonlinearities [10]. This implies that when the fluid velocity surpasses a critical threshold, the flag structure undergoes self-induced, self-sustaining oscillations of constant amplitude, known as limit cycle oscillations (LCO) [11]. Typically, this type of flutter-based harvester is structurally simple, with low manufacturing and maintenance costs. However, an obvious disadvantage is its high critical inflow velocity, which limits its application in low-speed fluid environments [12]. To overcome this limitation, a cylinder shape bluff body can be added to the front end of the flexible plate to induce vortex-induced vibration (VIV) [13]. This modification allows the flexible flag to synchronize its vibration frequency with the vortex shedding frequency of the cylinder at lower fluid velocities, enabling periodic oscillations of flexible structure. However, the lock-in synchronization range for this configuration is usually narrow [14, 15], allowing efficient energy harvesting only within a very limited range of fluid velocities. Therefore, some studies have combined VIV with galloping by integrating shapes of cylinders and square prisms [16, 17]. This combination effectively broadens the workable velocity range of the energy harvester, enhancing its adaptability and efficiency. Additionally, researchers are exploring the impact of different bluff body shapes on the performance of energy harvesters. Shapes such as Y [18], D [19], funnel [20], and inverted C [21] types, by altering flow field characteristics and vortex generation mechanisms, can largely influence energy harvesting effectiveness. Researches on designing these shapes not only aim to improve energy harvesting efficiency but also seek to expand the practical application environment of piezoelectric energy harvesters.

In addition to the use of just single vortex generator to enhance the vibration of flexible piezoelectric flag, WIV has been shown to be effective at lower cut-in flow velocities and across a wider range of effective flow velocities, making it particularly suitable for energy harvesting systems [22, 23]. The most common WIV configurations involve tandem-arranged cylinders, where the downstream cylinder is attached to a flexible base that integrates piezoelectric modules. The wake vortexes shed by the upstream cylinder reattach to the downstream cylinder to amplify its vibrations [24]. Despite this configuration effectively enhancing system output power, its drawback lies in the typically large spacing required between the upstream and downstream cylinders, which ranges from 3 to 11 times the cylinder diameter (d) [25, 26, 27]. This makes it unsuitable for space-constrained applications. An alternative configuration involves attaching the upstream cylinder to a flexible base while fixing different bluff bodies with various

cross-sectional shapes—such as triangular, circular, square, D-shaped, and flat plates—downstream in the flow field [28]. Among these choices, the flat plate downstream configuration yields the best results while maintaining a smaller spacing between the upstream and downstream elements. This approach not only improves space utilization but also optimizes vibration characteristics and energy harvesting efficiency by selecting suitable bluff body shapes. Beyond tandem cylinder designs, the effects of lateral spacing for two side by side cylinders have also been analyzed [29]. Adjusting the distance between the parallel cylinders can change the interaction of the shear layers in the wake, thereby influencing the vibration and energy harvesting of the flexible flag in their wake region.

Recently, a study proposed to replace the upstream vortex generator with double side by side arranged thin plates and connecting a downstream cylinder as a tip mass to the free end of a piezoelectric cantilever beam, with the trailing edge of the beam fixed [30]. This design reduces the spacing between the upstream and downstream vortex generators to $1d$. Due to the thinness of the plates, which are only 1/20 the diameter d of the downstream cylinder, their occupied space is negligible, further reducing the size of the WIV-type vortex generator. Furthermore, compared to the single cylinder and tandem arranged cylinders wake harvesters, this design achieves a substantial increase in power output. However, in this study, the vibration of the piezoelectric structure is still driven by the mass of the vibrating cylinder, lacking an analysis of the combined effect of the double plates and cylinder as a synergistic vortex generator on the free oscillation of the flexible flag structure in the wake. To explore the direct impact of the synergistic vortex generator on the flexible flag, in this paper, we will fix both the upstream double plates and the downstream cylinder in the flow field. The front end of the flexible flag is attached to the cylinder, allowing it to oscillate freely in the wake vortexes. We further analyze how the rotational angles of the upstream symmetric plates affects the overall performance of the energy harvester. Through this approach, we aim to demonstrate how the synergistic effects between the dual plates and the cylinder influence the vibration characteristics and energy harvesting efficiency of the flexible piezoelectric flag. This will provide theoretical insights for the design of future energy harvesters that utilize multiple vortex generator combinations.

In this study, we will conduct a detailed investigation into the effects of the wake vortexes generated by a synergistic vortex generator, composed of upstream double plates at various angles and a downstream cylinder, on the vibration and energy harvesting efficiency of a flexible piezoelectric flag. Firstly, in Section 2, we will provide a comprehensive description of the geometric design and model parameters of the synergistic vortex generator. Following this, in Section 3, the simulation methods and the governing equations involved will be introduced. Section 4 presents the simulation results and related discussion and analysis, focusing on the impact of different double plate angles on the vibration characteristics and energy harvesting performance of the piezoelectric flag. To gain a better understanding of the vibration excitation mechanism of the synergistic vortex generator, we will discuss the performance of the piezoelectric flag when combined with the double plates and cylinder separately. Finally, in Section 5, the contributions and limitations of the current work will be summarized, which will provide a critical assessment of the synergistic energy harvester and suggesting avenues for future research.

2 Energy harvester's description and model parameters

In this section, the schematic of the ~~proposed~~ synergistic vortex generator based energy harvester is illustrated. As in Figure 1 (a), in this design, two symmetric angle-adjustable rigid plates are placed upstream of the rigid fixed cylinder. The only flexible structure in this fluid-structure-piezoelectric coupled system is the slender flag, which is embedded with piezoelectric components for vibration energy harvesting in fluid flow environment. The wake flows generated by the upstream double plates and downstream cylinder are wished to generate stronger vortexes to strengthen the fluid lift force on the flexible flag and increase the vibrational amplitude and frequency.

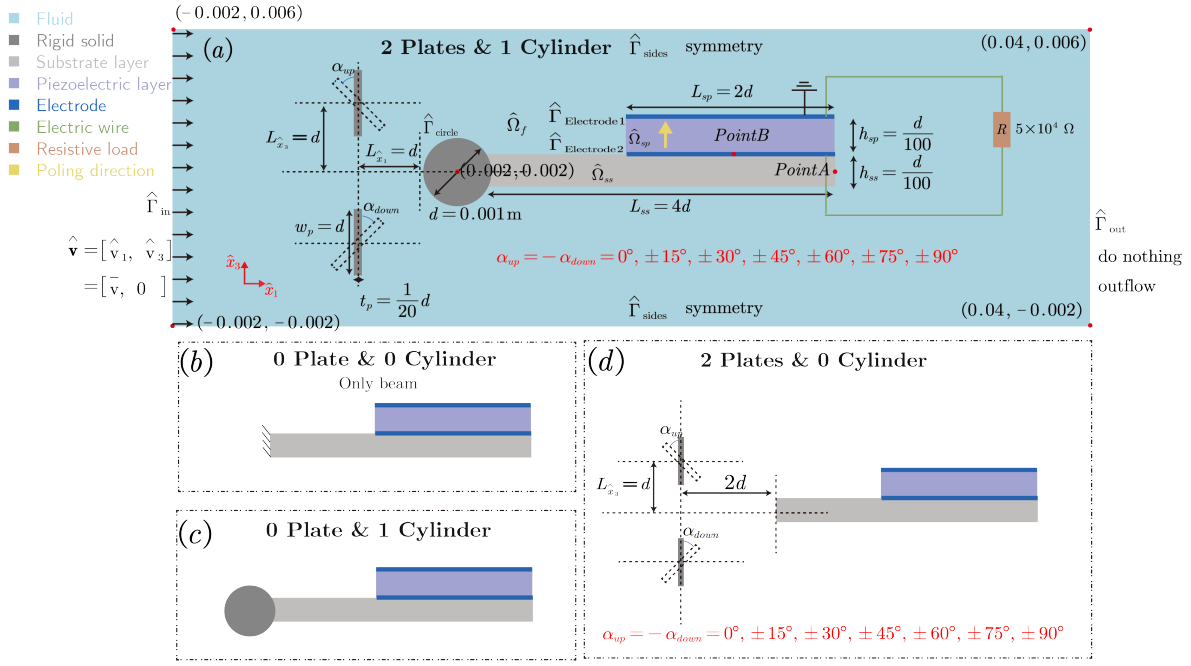

Figure 1: The designed synergistic vortex generator based energy harvester: geometry and boundary conditions of (a) 2 plates and 1 cylinder, (b) 0 plate and 0 cylinder, (c) 2 plates and 0 cylinder.

The material properties for the energy harvesting system components are listed in Table 1. The dimensions of the 2-D fluid domain, the base flag and the piezoelectric patch are specified as 0.042×0.008 m, 0.004×0.00001 m, and 0.002×0.00001 m in the $\hat{x}_1$ and $\hat{x}_3$ directions, respectively. The diameter d of the rigid cylinder is 0.001 m. Both the two upstream plates share the same width $w_p = d = 0.001$ m, and the thickness $t_p = d/20 = 0.00005$ m. The spacing between the center of two plates is set to be $\Delta G = 2L_{\hat{x}_3} = 2d = 0.002$ m as recommended in [31] for ensuring significant wake interaction between the double plates, otherwise the vortexes shedding from the plates would become independent of each other. The horizontal distance between the centers of double plates and the front of the cylinder is $L_{\hat{x}_1} = d = 0.001$ m. The varying parameter in this study is the angles of the double plates $\alpha_{up} = -\alpha_{down} = 0°, \pm 15°, \pm 30°, \pm 45°, \pm 60°, \pm 75°, \pm 90°$, and in the following sections the α_{up} will be used to identify each case for the sake of clarity. For each angle configuration, the upstream double plates and down stream cylinder are represented as fixed no-slip wall boundaries within the fluid domain.

Table 1: Material composition of the coupled system

Domains	Parameters	Values
$\widehat{\Omega}_f$ (Water)	ρ_f (kg/m^3)	1000
	μ_f (kg/(m $\cdot$ s))	0.001
	$\overline{\mathrm{v}}$ (m/s)	0.17
$\widehat{\Omega}_{ss}$ (Aluminum alloy)	ρ_{ss} (kg/m^3)	2800
	c_{11} (GPa)	112
	c_{22} (GPa)	60.5
$\widehat{\Omega}_{sp}$ (PZT5A)	ρ_{sp} (kg/m^3)	7750
	c_{11} (GPa)	120.35
	c_{13} (GPa)	75.09
	c_{33} (GPa)	110.9
	c_{44} (GPa)	21.05
	e_{15} (C $\cdot$ m^{-2})	12.29
	e_{31} (C $\cdot$ m^{-2})	-5.35
	e_{33} (C $\cdot$ m^{-2})	15.78
	ϵ_{11} (C $\cdot$ V^{-1})	8.14×10^{-9}
	ϵ_{33} (C $\cdot$ V^{-1})	7.32×10^{-9}
	R (Ω)	50000

For the piezo-part, electrodes are positioned at the upper and lower surfaces of the piezoelectric patch, with $\widehat{\Gamma}_{\text{Electrode1}}$ connected to the ground. A wire linking the two electrodes introduces a resistor with a resistance value of $5 \times 10^4\,\Omega$. Control points for result extraction are assigned to Point A, located at the center of the right end of the base structure, and Point B, at the center of the lower surface of the piezoelectric patch $\widehat{\Gamma}_{\text{Electrode1}}$. The fluid domain's inflow boundary is characterized by a uniform velocity, $\widehat{\mathrm{v}}_1 = \overline{\mathrm{v}}$, set at 0.17 m/s, which leads to the Reynold number $\mathrm{Re} = \rho_f \overline{\mathrm{v}} d/\mu_f = 170$. Symmetry boundary conditions are applied to the top and bottom sides, while a zero normal stress condition is enforced at the outflow. The surface of the circular bluff-body adheres to a no-slip boundary condition. To discretize the monolithic fluid-structure coupled system used in this study, which will be presented in Section 3, triangular finite elements are used throughout the domains, as illustrated in Figure 2. The mesh is constructed as a unified structure, with distinct markers identifying different domains. This setup ensures that interfaces between domains share the same nodes, facilitating accurate simulations. The total number of elements in this reference case is about 40000.

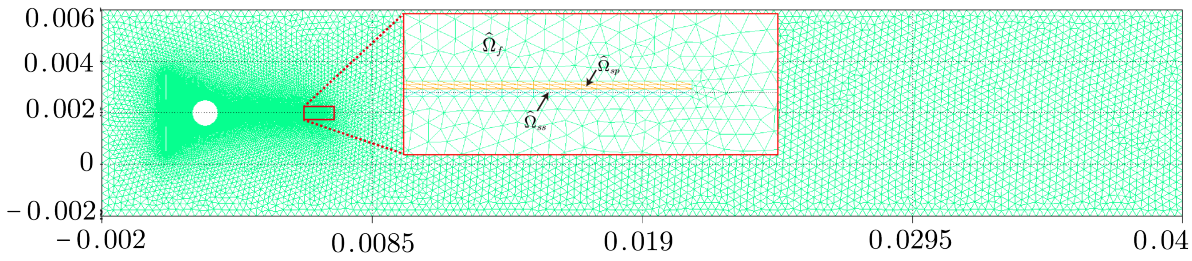

Figure 2: The fluid-structure-piezoelectric coupled system: computational mesh.

In order to further investigate the synergistic effect of the combination of multiple vortex generators, the analysis process is divided into four series of cases: 1) only flag with piezoelectric patch (0 plate & 0 cylinder in Figure 1 (b)); 2) cylinder-based energy harvester (0 plate & 1 cylinder in Figure 1 (c)); 3) double-plate-based energy harvester (2 plates & 0 cylinder in Figure 1 (d)); 4) synergistic energy

harvester (2 plates & 1 cylinder in Figure 1 (a)). All of these cases will share the same computational domain, with the only differences being the presence of upstream rigid double plates with different angles and the downstream rigid cylinder.

3 Governing equations

The fluid-structure-piezoelectric coupling problem illustrated in Figure 1 will be solved using a monolithic framework as proposed in our previous work [32]. This framework encompasses the surrounding fluid environment $\widehat{\Omega}_f$, the cantilever base structure $\widehat{\Omega}_{ss}$, and the attached piezoelectric patch $\widehat{\Omega}_{sp}$, along with an electric circuit that includes a resistance and electrodes in the initial undeformed state (reference configuration). In the following sections, we will detail the field equations and coupling conditions that govern the dynamics of this multiphysics system.

3.1 Equations of fluid dynamics

The fixed vortex generators and flexible flag are all surrounded by a incompressible viscous flow fluid, which is governed by the N-S equations in the Arbitrary Lagrangian-Euler (ALE) frame:

$$\rho_f \widehat{\boldsymbol{J}}_{\mathrm{A}} \frac{\partial \widehat{\mathbf{v}}_f}{\partial t} + \rho_f \widehat{\boldsymbol{J}}_{\mathrm{A}} \widehat{\mathbf{F}}_{\mathrm{A}}^{-1} \left(\widehat{\mathbf{v}}_f - \frac{\partial \widehat{\mathbf{u}}_{\mathrm{A}}}{\partial t} \right) \cdot \widehat{\nabla} \widehat{\mathbf{v}}_f = \widehat{\nabla} \cdot \left(\widehat{\boldsymbol{J}}_{\mathrm{A}} \widehat{\boldsymbol{\sigma}}_f \widehat{\mathbf{F}}_{\mathrm{A}}^{-\mathbf{T}} \right), \quad \text{in } \widehat{\Omega}_f, \tag{1}$$

$$\widehat{\nabla} \cdot \left(\widehat{\boldsymbol{J}}_{\mathrm{A}} \widehat{\mathbf{F}}_{\mathrm{A}}^{-1} \widehat{\mathbf{v}}_f \right) = 0, \qquad \text{in } \widehat{\Omega}_f, \tag{2}$$

where ρ_f and $\widehat{\mathbf{v}}_f$ are the fluid density and velocity. An auxiliary displacement field $\widehat{\mathbf{u}}_{\mathbf{A}}$, is introduced as $\widehat{\mathbf{u}}_{\mathrm{A}}(\widehat{\mathbf{x}}, t) = \mathbf{x} - \widehat{\mathbf{x}} = \widehat{\mathcal{A}}(\widehat{\mathbf{x}}, t) - \widehat{\mathbf{x}}$ to facilitate the transition of the fluid equations between the current and the reference configurations, where $\mathbf{x}$ and $\widehat{\mathbf{x}}$ is the coordinate in the deformed and undeformed domain. The deformation gradient $\widehat{\mathbf{F}}_{\mathrm{A}}$ is defined as $\widehat{\nabla} \widehat{\mathbf{u}}_{\mathrm{A}} + \mathbf{I}$, and $\widehat{\boldsymbol{J}}_{\mathrm{A}} = \det(\widehat{\mathbf{F}}_{\mathrm{A}})$ is its determinant. $\widehat{\boldsymbol{\sigma}}_f$ is the fluid stress tensor with Newtonian fluid constitutive law:

$$\widehat{\boldsymbol{\sigma}}_f = \widehat{\boldsymbol{\sigma}}_{fp} + \widehat{\boldsymbol{\sigma}}_{fv} = -\widehat{p}_f \mathbf{I} + \rho_f \mu_f \left(\left(\nabla \widehat{\mathbf{v}}_f \right) \widehat{\mathbf{F}}_{\mathrm{A}}^{-1} + \widehat{\mathbf{F}}_{\mathrm{A}}^{-\mathrm{T}} \left(\nabla \widehat{\mathbf{v}}_f \right)^{\mathrm{T}} \right) . \tag{3}$$

where $\widehat{p}_f$ is the fluid pressure and μ_f is the fluid dynamic viscosity.

3.2 Equations of fluid mesh motion

Fluid structure interaction problems within the ALE framework also require the accurate modeling of fluid mesh movement. To address this, the auxiliary displacement field $\widehat{\mathbf{u}}_{\mathrm{A}}$, introduced earlier in Section 3.1, is utilized to extend structural deformations into the fluid domain. The auxiliary displacement field represents the motion of the fluid mesh without incorporating inertial effects. In this study, the biharmonic equation [33] is employed to govern mesh movement:

$$\widehat{\boldsymbol{\eta}}_{\mathrm{A}} = -\alpha_u \widehat{\Delta} \widehat{\mathbf{u}}_{\mathrm{A}}, \quad -\alpha_u \widehat{\Delta} \widehat{\boldsymbol{\eta}}_{\mathrm{A}} = 0, \quad \text{in } \widehat{\Omega}_f, \tag{4}$$

where $\widehat{\boldsymbol{\eta}}$ is an intermediate variable, and α_u is an artificial material parameter, typically determined empirically, that regulates the mesh motion.

3.3 Equations of motion of the elastic structure

The equation governing the balance of linear momentum for a solid continuum considering large deformations in the Lagrangian coordinate system relative to the reference configuration $\widehat{\Omega}_{ss}$, is:

$$\rho_{ss}\frac{\partial^2\widehat{\mathbf{u}}_{ss}}{\partial t^2}-\widehat{\nabla}\cdot\widehat{\boldsymbol{\Pi}}_{ss}=0,\quad \text{in } \widehat{\Omega}_{ss}. \tag{5}$$

where ρ_{ss} is the density of the elastic solid, $\widehat{\boldsymbol{\Pi}}_{ss}$ denotes the First Piola-Kirchhoff stress tensor, which is often given as the function: $\widehat{\boldsymbol{\Pi}}_{ss}=\widehat{\mathbf{F}}_{ss}\widehat{\boldsymbol{\Sigma}}_{ss}$. $\widehat{\mathbf{F}}_{ss}=\mathbf{I}+\widehat{\nabla}\widehat{\mathbf{u}}_{ss}$ is the deformation gradient, and Second Piola-Kirchhoff stress tensor $\widehat{\boldsymbol{\Sigma}}_{ss}$ is given by:

$$\widehat{\boldsymbol{\Sigma}}_{ss}=\mathbb{C}_{ss}:\widehat{\mathbf{S}}_{ss}\,, \tag{6}$$

using the linear elastic material with the fourth-order elasticity tensor $\mathbb{C}_{ss}$ and the Green–Lagrange strain tensor $\widehat{\mathbf{S}}_{ss}=\frac{1}{2}\left(\widehat{\mathbf{F}}_{ss}^{\mathrm{T}}\widehat{\mathbf{F}}_{ss}-\mathbf{I}\right)$. In the monolithic FSI coupling, the primary variable used for structure is the velocity $\widehat{\mathbf{v}}_{ss}$ rather than the displacement $\widehat{\mathbf{u}}_{ss}$ for the geometrical compatibility. Therefore, we have the relationship:

$$\partial\widehat{\mathbf{v}}_{ss}=\frac{\partial\widehat{\mathbf{u}}_{ss}}{\partial t}\,. \tag{7}$$

3.4 Equations of motion of the piezoelectric structure

Piezoelectricity involves the interaction between mechanical and electrical phenomena. Consequently, the governing equations are the momentum conservation for the mechanical field and the Gauss's equation for the electric field in the domain $\widehat{\Omega}_{sp}$ with respect to the reference configuration:

$$\rho_{sp}\frac{\partial^2\widehat{\mathbf{u}}_{sp}}{\partial t^2}-\widehat{\nabla}\cdot\widehat{\boldsymbol{\Pi}}_{sp}=0,\quad \text{in } \widehat{\Omega}_{sp}\,, \tag{8}$$

$$\widehat{\nabla}\cdot\widehat{\mathbf{D}}_{sp}=0,\quad \text{in } \widehat{\Omega}_{sp}\,, \tag{9}$$

where ρ_{sp} represents the density of the piezoelectric solid. Unlike the purely elastic solid by Eq. (5), the first Piola-Kirchhoff stress tensor of $\widehat{\Omega}_{sp}$ in the reference configuration, $\widehat{\boldsymbol{\Pi}}_{sp}=\widehat{\mathbf{F}}_{sp}\widehat{\boldsymbol{\Sigma}}_{sp}$, involves piezoelectric effect and results from both displacement $\widehat{\mathbf{u}}_{sp}$ and potential $\widehat{\boldsymbol{\varphi}}_{sp}$. $\widehat{\mathbf{D}}_{sp}$ represents the electric displacement. $\widehat{\mathbf{F}}_{sp}=\mathbf{I}+\widehat{\nabla}\widehat{\mathbf{u}}_{sp}$ is the deformation gradient, and the constitutive equations are as follows:

$$\widehat{\boldsymbol{\Sigma}}_{sp}=\mathbb{C}_{sp}:\widehat{\mathbf{S}}_{sp}+\mathbf{e}_{sp}\cdot\widehat{\mathbf{E}}_{sp}, \tag{10}$$

$$\widehat{\mathbf{D}}_{sp}=\mathbf{e}_{sp}:\widehat{\mathbf{S}}_{sp}+\boldsymbol{\epsilon}_{sp}\cdot\widehat{\mathbf{E}}_{sp}\,. \tag{11}$$

where $\mathbb{C}_{sp}$ is the classical fourth-order elastic tensor; $\boldsymbol{\epsilon}_{sp}$ is the second-order tensor describing dielectric permittivity; and $\mathbf{e}_{sp}$ is the third-order piezoelectric coupling tensor; $\widehat{\mathbf{S}}_{ss}=\frac{1}{2}\left(\widehat{\mathbf{F}}_{ss}^{\mathrm{T}}\widehat{\mathbf{F}}_{ss}-\mathbf{I}\right)$ is the Green–Lagrange strain tensor and $\widehat{\mathbf{E}}_{sp}=-\widehat{\nabla}\widehat{\boldsymbol{\varphi}}_{sp}$ is the electric field. Similar to Section 3.4, velocity $\widehat{\mathbf{v}}_{sp}$ and displacement $\widehat{\mathbf{u}}_{sp}$ are also needed to be related with each other by the relationship:

$$\partial\widehat{\mathbf{v}}_{sp}=\frac{\partial\widehat{\mathbf{u}}_{sp}}{\partial t}\,. \tag{12}$$

3.5 Equations of Electrodes and circuit

To harvest the electrical energy generated through the direct piezoelectric effect from the deformation of the piezoelectric component $\widehat{\Omega}_{sp}$, it is necessary to integrate a closed external circuit to the system. In this study, this circuit includes a resistor of resistance R, connected via electric wires to the two electrodes of the piezoelectric component. Based on the Ohm's law and the definition of the electric current, the following electrode–circuit coupling equation holds:

$$\frac{\widehat{\boldsymbol{\varphi}}_{sp}^{\text{Electrode2}}}{R} = I = -\frac{\partial Q}{\partial t}\,, \quad \text{on}\,\widehat{\Gamma}_{\text{Electrode2}}, \tag{13}$$

where I denotes the current flowing through the circuit, and Q the total electric charges accumulated on the electrode-covered surfaces. The electrodes ($\widehat{\Gamma}_{\text{Electrode1}}$ and $\widehat{\Gamma}_{\text{Electrode2}}$ in Figure 1) considered here have a negligible thickness covering the surfaces of the piezoelectric solid structure, and they will ensure the equal potential conditions during vibrations. In the simulation process, $\widehat{\boldsymbol{\varphi}}_{sp}^{\text{Electrode2}}$ will be represented by $\widehat{\boldsymbol{\varphi}}_{sp}^{\text{PointB}}$.

3.6 Equations of fluid-structure interface

We carry out the FSI coupling by considering the two involved solid domains, $\widehat{\Omega}_{ss}$ and $\widehat{\Omega}_{sp}$, as a single entity, referred to as $\widehat{\Omega}_s$. Despite their distinct material compositions, the base plate and the piezoelectric component behave similarly when interacting with the surrounding fluid flow. The FSI interface between $\widehat{\Omega}_{ss} \cup \widehat{\Omega}_{sp}$ and the surrounding fluid is denoted as $\widehat{\Gamma}_{\text{FSI}}$, as indicated in Figure 1. At this interface, we ensure equilibrium by maintaining the continuity of displacement and velocity fields, as well as the normal components of the stress tensor, therefore:

$$\widehat{\mathbf{u}}_{\text{A}} = \widehat{\mathbf{u}}_s, \quad \text{on} \;\; \widehat{\Gamma}_{\text{FSI}} \tag{14}$$

$$\widehat{\mathbf{v}}_f = \widehat{\mathbf{v}}_{\text{A}} = \frac{\partial \widehat{\mathbf{u}}_s}{\partial t}, \quad \text{on} \;\; \widehat{\Gamma}_{\text{FSI}} \tag{15}$$

$$\left(\boldsymbol{J}_{\text{A}} \widehat{\boldsymbol{\sigma}}_f \mathbf{F}_{\text{A}}^{-\mathbf{T}}\right) \cdot \widehat{\mathbf{n}}_{\text{FSI}} = \widehat{\boldsymbol{\Pi}}_s \cdot \widehat{\mathbf{n}}_{\text{FSI}}, \quad \text{on} \;\; \widehat{\Gamma}_{\text{FSI}} \tag{16}$$

where $\widehat{\mathbf{n}}_{\text{FSI}}$ is the normal vector at the FSI interface. We apply the convention that $\widehat{\mathbf{n}}_{\text{FSI}}$ points from $\widehat{\Omega}_f$ towards $\widehat{\Omega}_s$.

3.7 Solution scheme

The resolution of the fluid-structure-piezoelectric coupling problem involving Eqs. (1) to (16) is based on the monolithic solution approach. The Galerkin finite element method is used for the space discretization and the One-Step-θ method is used for the time discretization. Specific details can be found in our previous work [32].

With the governing equations and settings above, all simulations in this study were performed using the open-source environment, FEniCS [34] and its extension, TurtleFSI [35]. TurtleFSI is a FEniCS extension designed for general fluid-structure interaction problems. In this work, TurtleFSI has been extended to accommodate more complex coupled problems, such as the integration of fluid-structure-piezoelectric coupling with an external electric circuit, as depicted in Figure 3.

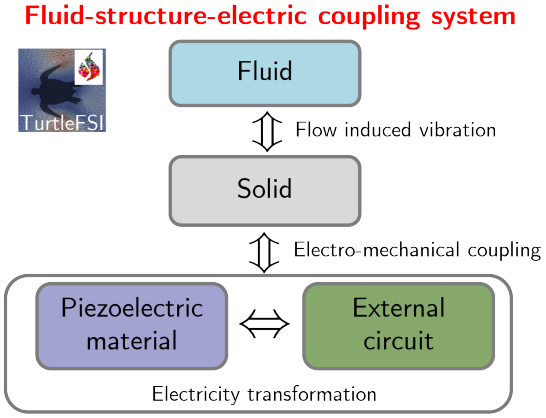

Figure 3: The relations between different components of the coupling system

4 Results and discussions

In the previous section, we described the geometric design, model parameters and governing equations of the ~~newly proposed~~ synergistic energy harvester in dynamic fluid environment. In this section, we will focus on analyzing the impact of the synergistic effects of multiple vortex generators on the energy harvester, based on the results of numerical simulations. To achieve this, we first need to explore the individual characteristics of the different vortex generators in the fluid-structure-piezoelectric coupled system, i.e. fixed rigid cylinder or double plates. This will allow us to better comprehend the combined effects when these components are integrated. We will begin by investigating the scenario with only the piezoelectric flag. Subsequently, the piezoelectric flag will be combined separately with a rigid cylinder or double plates at different rotational angles. Finally, we will analyze the flow field characteristics, the dynamic response of the piezoelectric energy harvesting flag, and its energy harvesting performance in the presence of both the rigid cylinder and the double plates. These simulation results will demonstrate the superiority of the synergistic energy harvester, specifically in terms of the enhancements in vibration amplitude, frequency, and stability of the piezoelectric flag.

4.1 Flag only energy harvester and cylinder-based energy harvester

In an energy harvester without upstream vortex generators, the vibration of the flexible flag depends on the flutter mechanism for energy harvesting. The flag initiates self-induced oscillation only when the fluid velocity exceeds a critical threshold [3]. However, under the flow conditions described in this study, the fluid velocity is relatively low, preventing the flag from vibrating, as shown in Figures 4(a) and 6(a). As a result, the system is unable to convert fluid kinetic energy into electrical energy.

When a fixed rigid cylinder is added to the leading edge of the piezoelectric flag, the vibration mechanism of the energy harvester transitions from flutter to vortex-induced vibration (VIV). VIV is characterized by alternating vortex shedding at relatively low flow velocities or Reynolds numbers, as illustrated by the streamline pattern in Figure 4(b). These alternating vortices create a pressure differential on either side of the flexible flag downstream (as shown in Figure 5(b)), leading to periodic

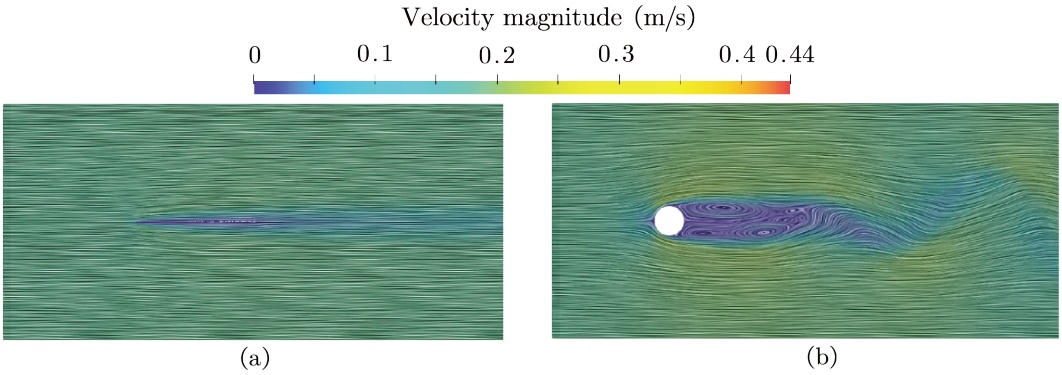

Figure 4: Velocity contours with streamline for (a) flag only energy harvester and (b) cylinder-based energy harvester.

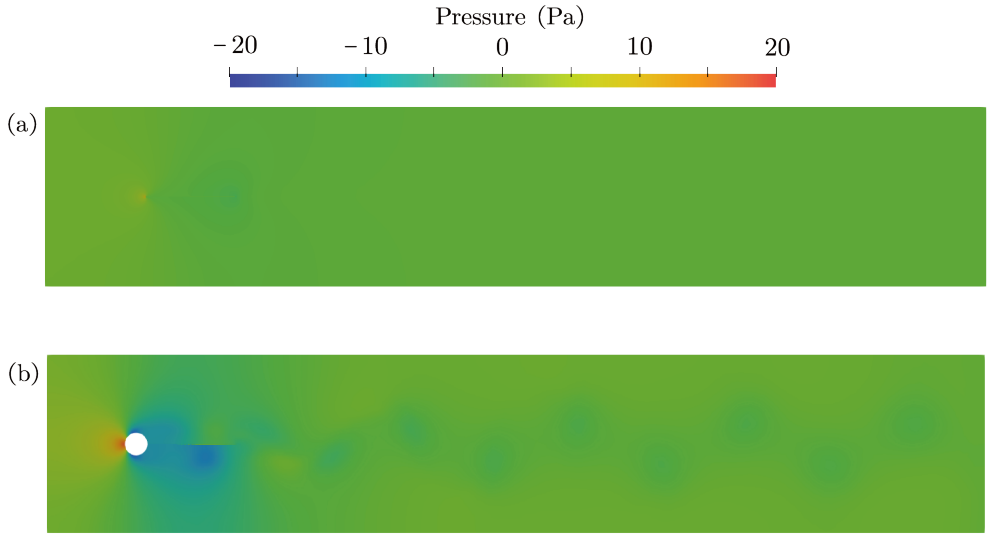

Figure 5: Pressure contours for (a) flag only energy harvester and (b) cylinder-based energy harvester.

vibrations of the structure.

In the cylinder-based energy harvester, the vibration mode of the flexible flag is typically influenced by the normalized stiffness ($K_b = Eh^3/(12\rho_f \bar{\mathrm{v}}^2 L^3)$, where E, h, L are the Young's modulus, the flag thickness and the flag length, respectively) [36]. In our case, the flag predominantly exhibits a stable vibration in limit cycle oscillation (LCO) with first-mode type, as depicted in Figure 6(b) and (d), because of the rather high $K_b = 3.15$. This mode would be suitable for energy harvesting because higher-order mode shapes are often associated with strain nodes causing strong cancellations of the electrical outputs, which can negatively impact the voltage output of the piezoelectric material [37].

In the subsequent case studies, maximum vibration amplitude $\widehat{\mathrm{u}}_{3,\max}$, vibration frequency f of Point A on the flag free end, and the averaged energy harvesting power, efficiency of the cylinder-based energy harvester, will be used as reference for comparison with other types of energy harvesters, as listed in Table 2. Here the definition of energy harvesting efficiency comes from [38], which is expressed as $\text{Efficiency} = \frac{\text{AveragedPower}}{0.5\rho_f \bar{\mathrm{v}}^3 (2\widehat{\mathrm{u}}_{3,\max})}$.

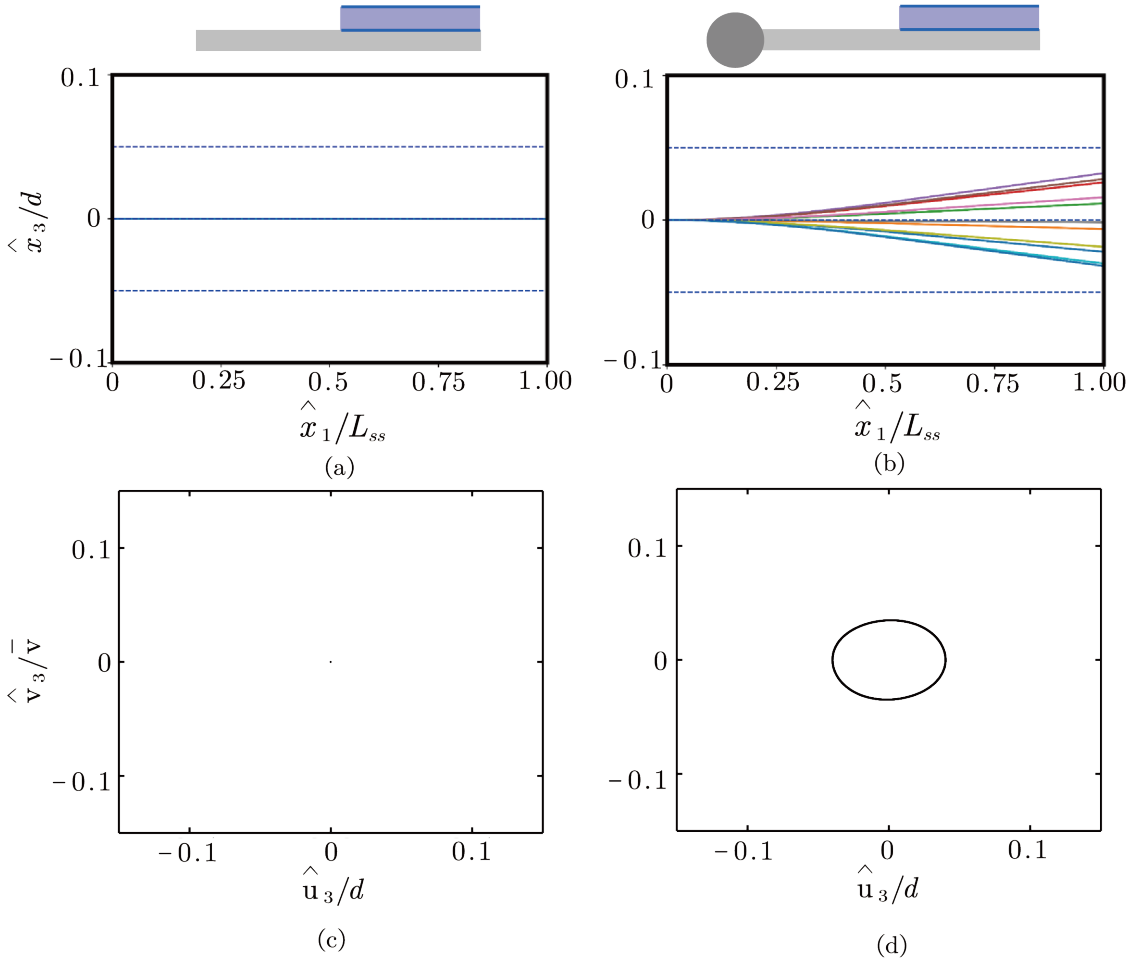

Figure 6: The full-body responses and phase plane trajectories for (a)(c) only flag energy harvester and (b)(d) cylinder-based energy harvester.

Table 2: Statistic data for cylinder-based energy harvester.

Case name	f (Hz)	$\hat{u}_{3,\max}/d$	Averaged Power (W)	Efficiency (%)
0 plate & 1 cylinder	23.8	0.04	4.24×10^{-10}	2.15×10^{-4}

4.2 Double-plate-based energy harvester

We next examine the impact of upstream double plates with variable angles α_{up}, on the energy harvesting behavior of the piezoelectric flag in the flow field. As shown in Figure 7, the wake flow states can be classified into three distinct types: (1) The first type is the asymmetric wake flow, corresponding to plate angles α_{up} ranging from -30° to 0°. In this condition, the alternating vortex shedding from the upstream plates is asynchronous. And combined with the interaction of the flag vibration, it forms a rather irregular and asymmetric wake flow. (2) The second type occurs when the plate angle α_{up} range from -60° to -45° and 15° to 60°. The upstream double plates produce completely symmetric and synchronous vortex shedding. At the same time, the flexible flag generates extremely weak vibrations compared to the first type, which has small impact on the wake flow and exhibits a highly symmetrical wake form. (3) The third type arises when the plate angle α_{up} is too large, less than -75° and greater than 75°. In this case, the upstream double plates will not produce shedding vortex, and there is no interaction between upstream double plates and downstream flexible flag. Consequently, the vibration mechanism of the downstream plates reverts to flutter. As with the result of only flag energy harvester in Section 4.1, the flexible flag will not vibrate in this inflow velocity.

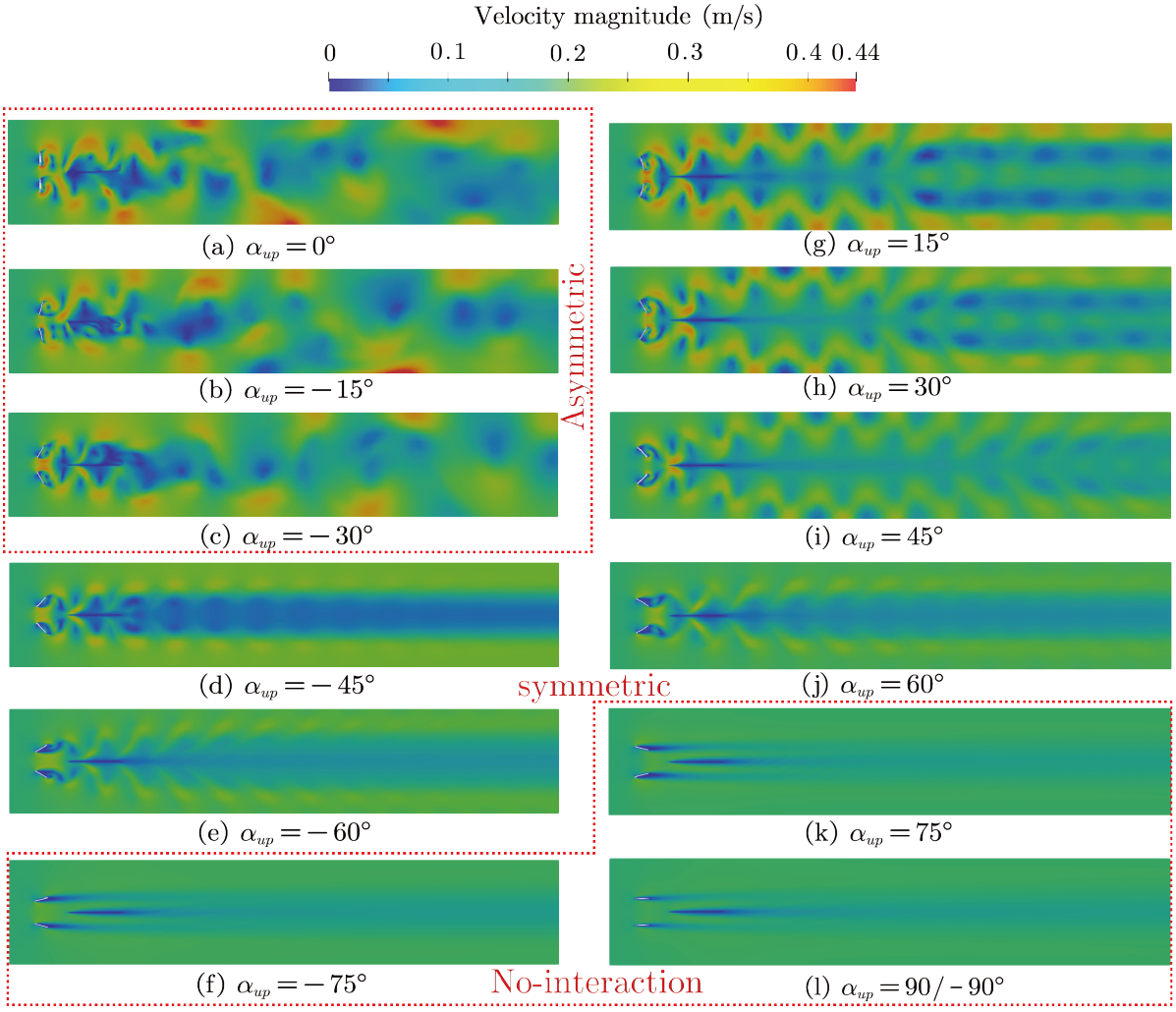

Figure 7: Velocity contours for double-plate-based energy harvester with different α_{up}.

In Figures 8 and 9, the vortex shedding and development processes after the double plates are further presented for the first two kinds of wake types. We use black circles to mark two pairs of vortexes generated after the double plates. And it is noted that v1 and v2 represent a pair of vortexes shed from the upper plate, while v3 and v4 are from the lower plate. v1 and v3 rotate clockwise, whereas v2 and v4 rotate counterclockwise.

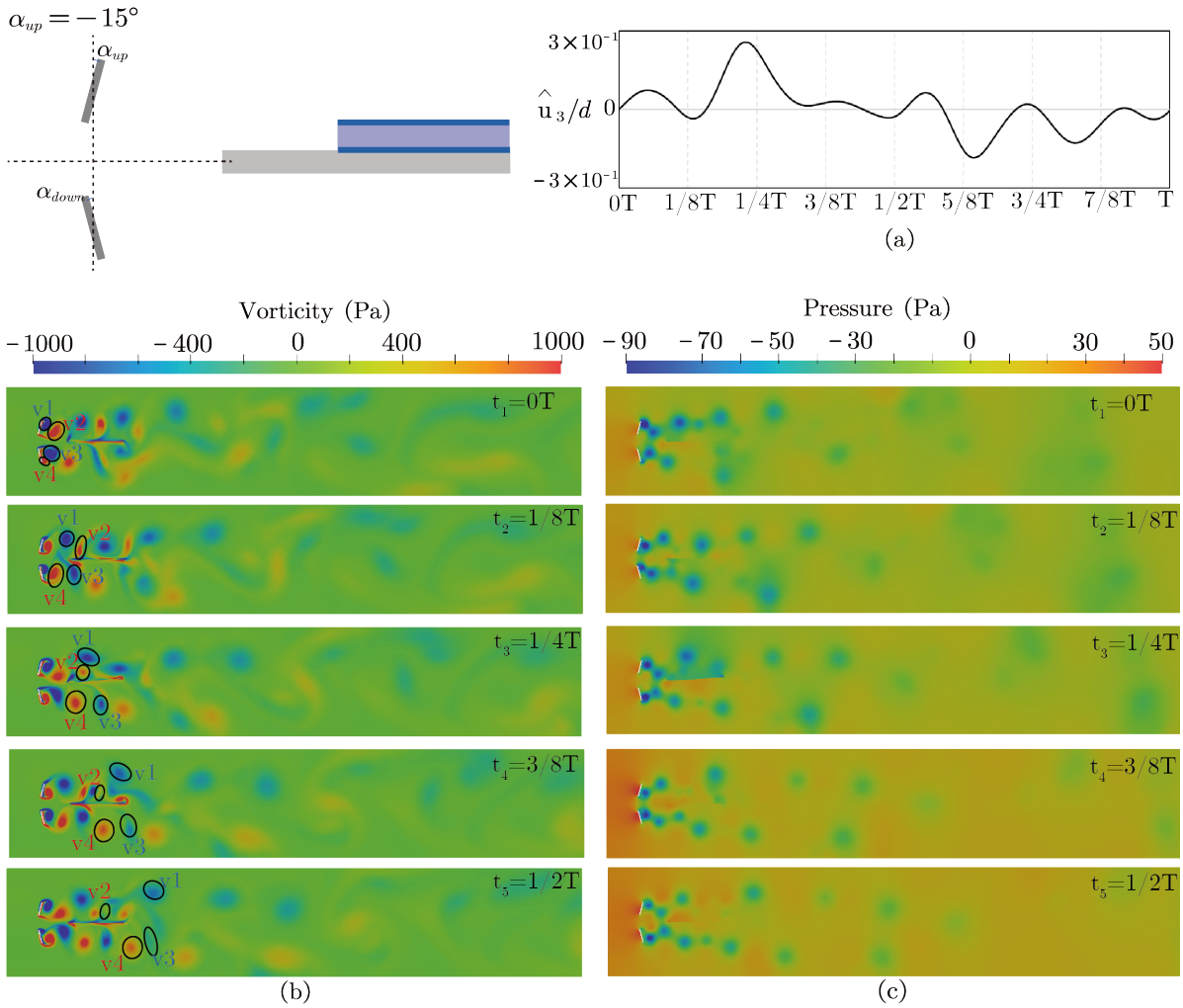

Figure 8: Flow field development process of double-plate-based energy harvester when $\alpha_{up} = -15°$.

When $\alpha_{up} = -15°$, as illustrated in Figure 8, we select five time nodes from the first half of the vibration cycle to display the transient vortex and pressure contours of the flow field. At time t_1, two pairs of vortexes are generated behind the two rigid plates. During time range t_1 to t_2, these vortex pairs move from the double plates towards the head of the flexible flag, with v1 and v2 moving slightly faster than v3 and v4. However, after time t_2, the movement speeds of v1 and v2 noticeably slow down compared to v3 and v4. The slower-moving vortexes on the upper side of the flexible flag are closer to the structure, forming a continuous negative pressure zone at time t_3. Correspondingly, the vortexes on the lower side of the flag are farther away, creating a positive pressure zone underneath the flag, which generates an upward lift force causing the flag to deform upwards. At time t_4, v1 and v2 has begun to merge with other surrounding vortexes, and by the time t_5, they already approach dissipation. At

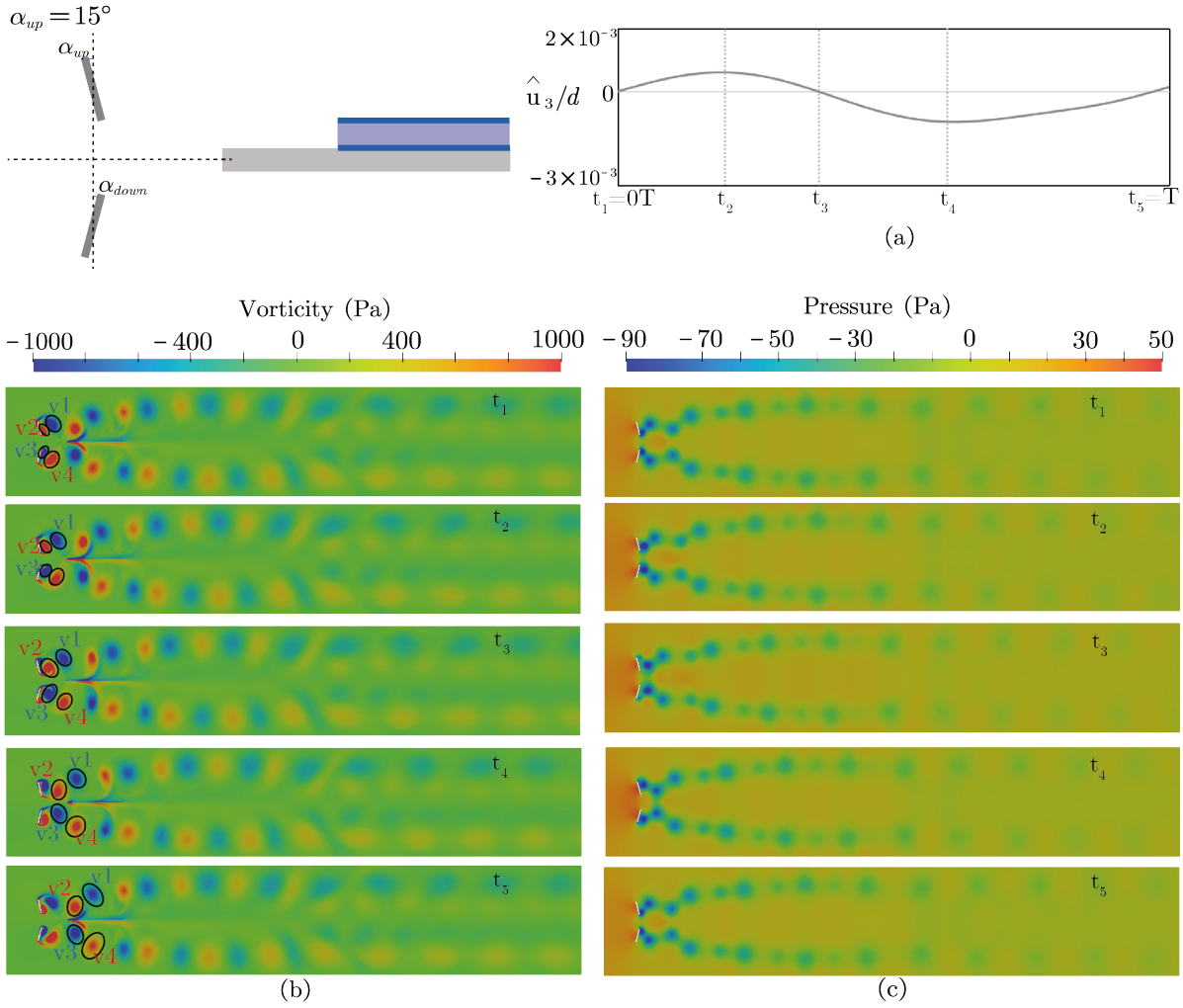

Figure 9: Flow field development process of double-plate-based energy harvester when $\alpha_{up} = 15°$.

this point, newly generated vortexes begin to act on the flag, causing the positive and negative pressure zones on the upper and lower sides of the flag to switch. This generates a downward lift force, causing the flag to begin deforming downward.

The situation is entirely different in the second type of wake when $\alpha_{up} = 15°$. As illustrated in Figure 9, we display vortex and pressure contours at five time nodes within one vibration cycle. It can be observed that at different moments, v1 and v4, as well as v2 and v3, are symmetrical about the centerline of the flow field. This symmetrical votex shedding results in nearly identical flow pressure conditions on both the upper and lower sides of the flexible flag, preventing the formation of a significant pressure differential. Consequently, the vibration amplitude of the flag is reduced by two orders of magnitude compared to that of case with $\alpha_{up} = 15°$, as shown in Figures 9(a) and 8(a).

Then, by comparing the phase plane trajectories at Point A and the full-body response snapshots of the flag within the vibration cycles for three cases of the cylinder-based energy harvester with asymmetric wake flow, as shown in Figure 10, it can be observed that the vibration amplitude of the flexible flag is significantly enhanced when using the double plates vortex generators. But the parasitic cost is the decrease of vibration stability. Different from Figure 10(a), where the phase plot of cylinder

based energy harvester keeps a typical limit-cycle trajectory, plots in the phase plane for the other three cases of double-plate-based energy harvester do not trend to a specific trajectory, but tend to be unstable and chaotic. Figure 11 compares the time-domain results between the three cases with asymmetric wake flows and the cylinder-based case. The comparison includes the displacement $\widehat{u}_3$ at Point A, the potential output at Point B, and the lift force exerted by the fluid on the entire flexible flag. It can be observed that for the cylinder-based energy harvester, the results stabilize into a periodic oscillation with constant amplitude after a normalize time $t\overline{v}/L_{ss}$ greater than 30. However, for the double-plate-based cases, the amplitude in the time-domain results continuously varies and occasionally exhibits sudden increases. This phenomenon leads to unstable power output and negatively affects the average power output.

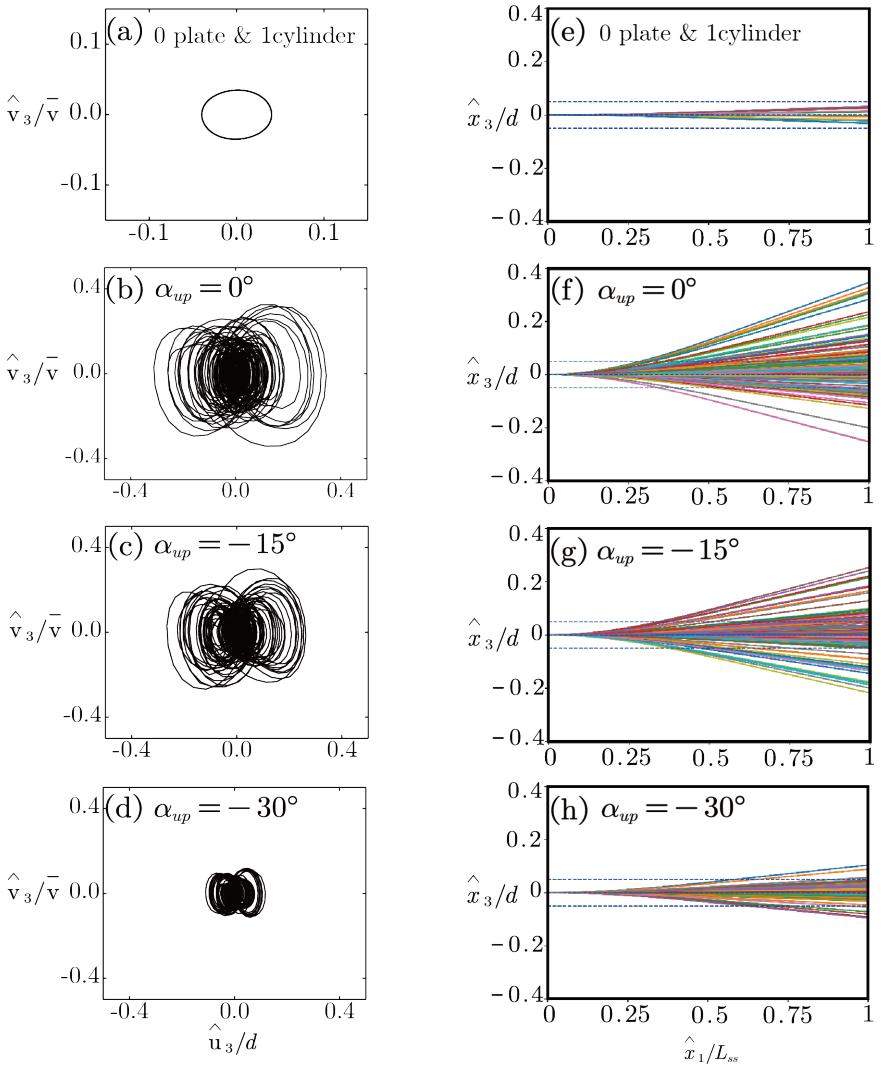

Figure 10: The phase plane trajectories and full-body responses for (a)(e) cylinder-based energy harvester and double-plate-based energy harvester (b)(f) $\alpha_{up} = 0°$, (c)(g) $\alpha_{up} = -15°$, (d)(h) $\alpha_{up} = -30°$.

Figure 12 presents the statistical results for the double-plate-based energy harvester with different upstream plate angles α_{up}. The dashed lines represent the cylinder-based case results. For the cases

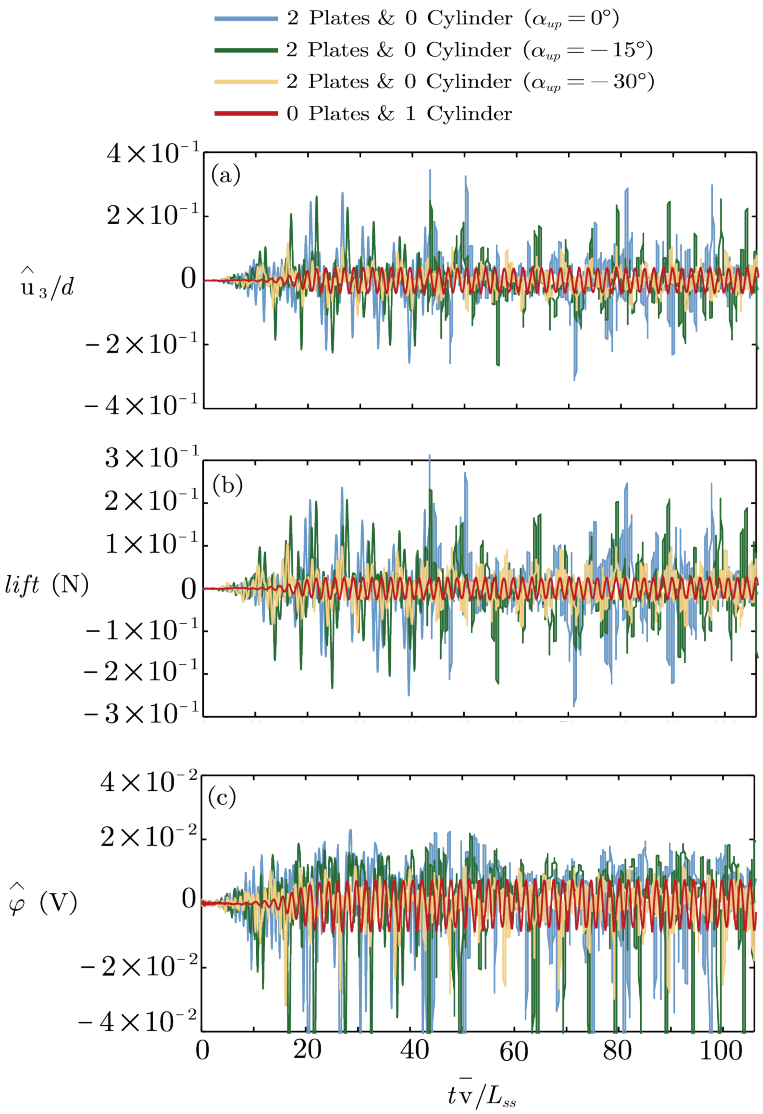

Figure 11: Time history of (a) displacement $\widehat{u}_3$ of Point A in $\widehat{x}_3$ direction, (b) lift force of the flag (without the rigid parts), (c) the potential $\widehat{\phi}$ of Point B for cylinder-based energy harvester and double-plate-based energy harvester where $\alpha_{up} = 0°, -15°, -30°$.

with α_{up} ranging from -30° to 0°, both the maximum vibration amplitude of the flag free end $\widehat{u}_{3,\max}$ and the average power output of the structure show significant increases, but the vibration frequency f is notably reduced by 71% to 6.9 Hz. Here based on the definition of energy harvesting efficiency $\text{Efficiency} = \frac{\text{AveragedPower}}{0.5\rho_f \bar{v}^3 (2\widehat{u}_{3,\max})}$, it will result in a decrease in the energy harvesting efficiency of the system when the increase of average power is smaller than the increase in vibration amplitude compared to the reference cylinder-based case as shown in Figure 12(d). This is because the vibration amplitudes of the three cases ($\alpha_{up} = 0°, -15°, -30°$) keep changing and cannot consistently maintain their biggest value, for example $\widehat{u}_{3,\max} = 0.328d$ when $\alpha_{up} = 0$, as shown in Figure 11(a). And consequently, this variability in vibration amplitude negatively impacts the average power output of the energy harvester together with the decreased frequency f.

Overall, for double-plate-based energy harvester, by adjusting the angle of the upstream plates, we can obtain an asymmetric wake flow pattern to create larger lift force acting on the piezoelectric flag to

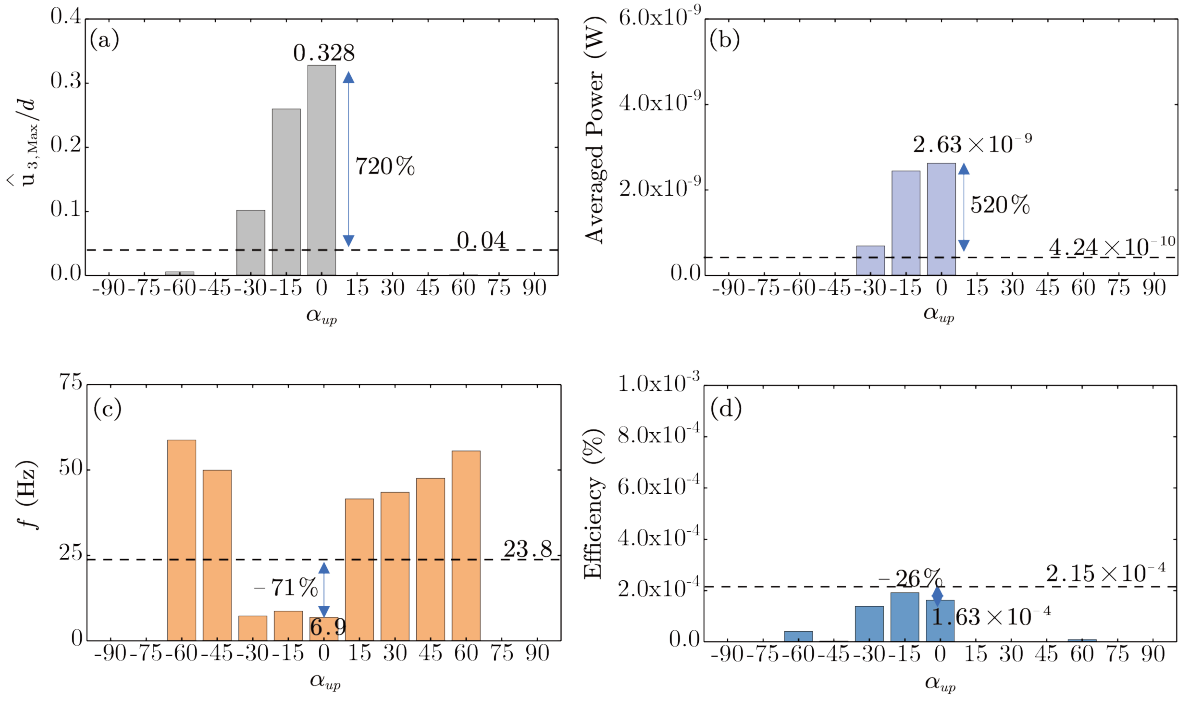

Figure 12: Statistic results of double-plate-based energy harvester with different α_{up}: (a) the maximum value of displacement $\hat{u}_3$ of Point A in $\hat{x}_3$ direction, (b) the averaged power, (c) the vibration frequency, (d) the energy harvesting efficiency.

increase the power output comparing to cylinder-based energy harvester. Nevertheless, the reduction in the vibration frequency and the inability to maintain large amplitude vibrations consequently result in a noticeable decrease in the energy harvesting efficiency of this type of energy harvester and impose restrictions on further enhancement of energy harvesting behavior.

4.3 Synergistic energy harvester

The flow field characteristics and the effects on the piezoelectric flexible flag imposed by the cylinder vortex generator and the double-plate vortex generator have been analyzed independently in Sections 4.1 and 4.2. Each vortex generator has its own advantages: the rigid cylinder induces stable VIV with relatively small amplitude, while the double plates generate stronger vortexes that induce large vibrations but with poor stability. To leverage their respective strengths, we will combine these two sets of vortex generators to form a synergistic vortex generator with different double-plate angles α_{up} range from $-90°$ to $90°$. We will then discuss in detail how this combination impacts the performance of the energy harvester.

In Figure 13, the wake characteristics of the flow field can be classified into two main types. The first type occurs when α_{up} is relatively small (ranging from $-30°$ to $45°$), and the wake exhibits a pattern similar to the double-plate wake presented in Section 4.2. In this scenario, the upper and lower plates generate corresponding upper and lower wake vortexes, forming an upper shear layer and a lower shear layer in the wake region, as indicated in Figure 14(a). Specifically, when the angles are $-15°$ and $30°$, the vortexes behind the two rigid plates shed asynchronously, resulting in an asymmetric wake pattern. For the other angles within the range of $-30°$ to $45°$, the vortexes in the upper and lower

wakes are symmetrically distributed along the centerline of the fluid domain.

The second main type occurs when α_{up} is larger (ranging from $-30°$ to $-90°$ and $45°$ to $90°$). The wake in this case resembles the Karman vortex street typical of a cylinder wake as also shown in Figure 14(b). When α_{up} is $-45°$ or $60°$, the vortexes shedding from the double plates interact with the cylinder wake vortexes, leading to a bigger vortex group around the flag. When $\alpha_{up} \leqslant -60°$ or $\alpha_{up} \geqslant 75°$, the effective block area of the double plates is too small to generate vortex shedding, thereby reducing the synergistic amplification effect with the downstream rigid cylinder vortex generator.

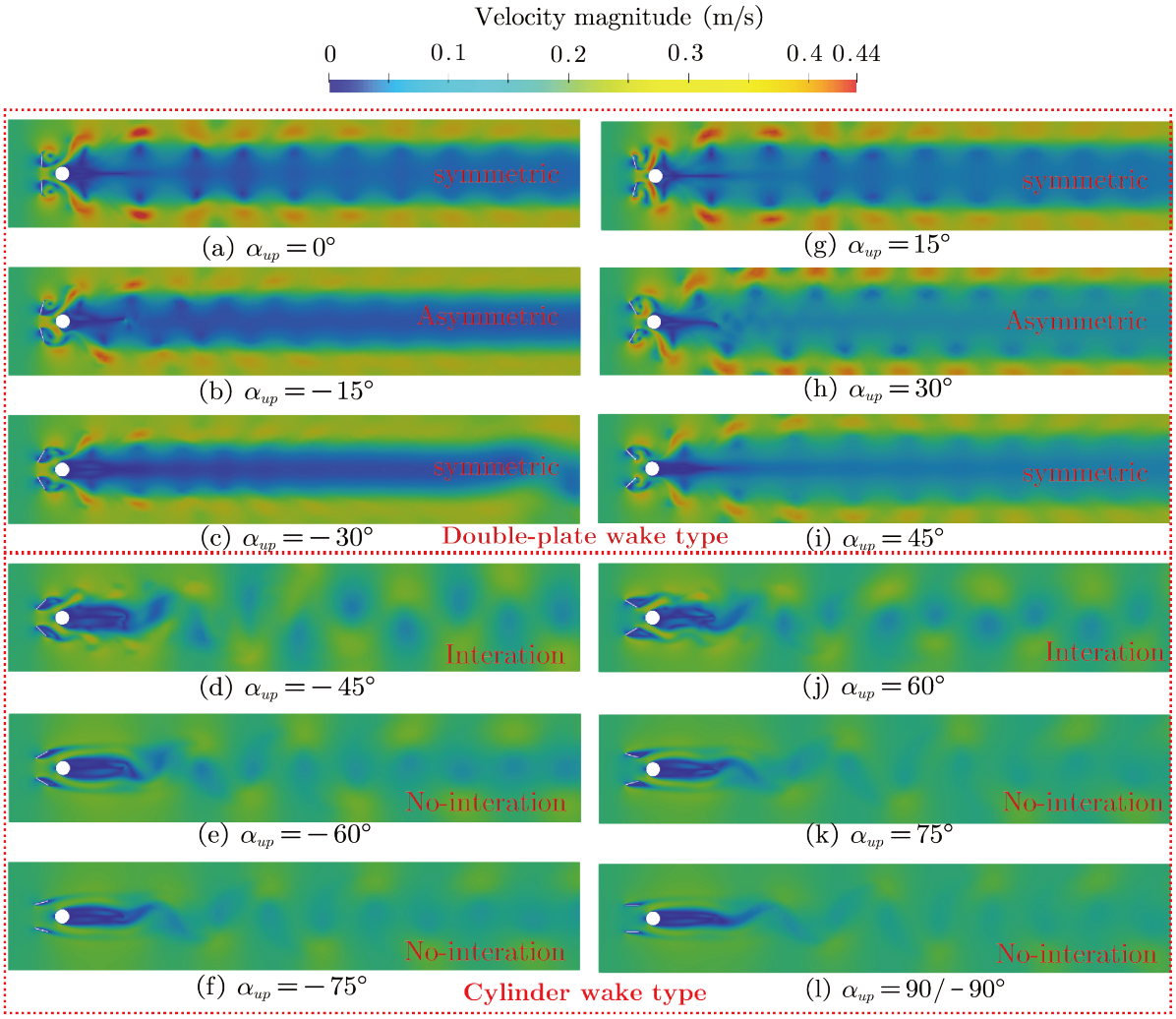

Figure 13: Velocity contours for synergistic energy harvester with different α_{up}.

Accordingly, we conducted further analysis of the instantaneous flow field development at four different α_{up}: $0°$, $-15°$, $-45°$, and $90°$. Figures 15-18 show the vortex and pressure contours at five different time nodes within one vibration cycle for different α_{up}. We still identified and marked the two pairs of vortexes shed behind the double plates, with v1 and v2 originating from the upper plate, and v3 and v4 from the lower plate.

In Figure 15, when $\alpha_{up} = 0°$, the two pairs of vortexes are generated synchronously on both upper and lower sides of the flow field and move downstream at the same speed. Consequently, the pressure contour plots at each time node will exhibit a symmetrical distribution, resulting in very small vibration

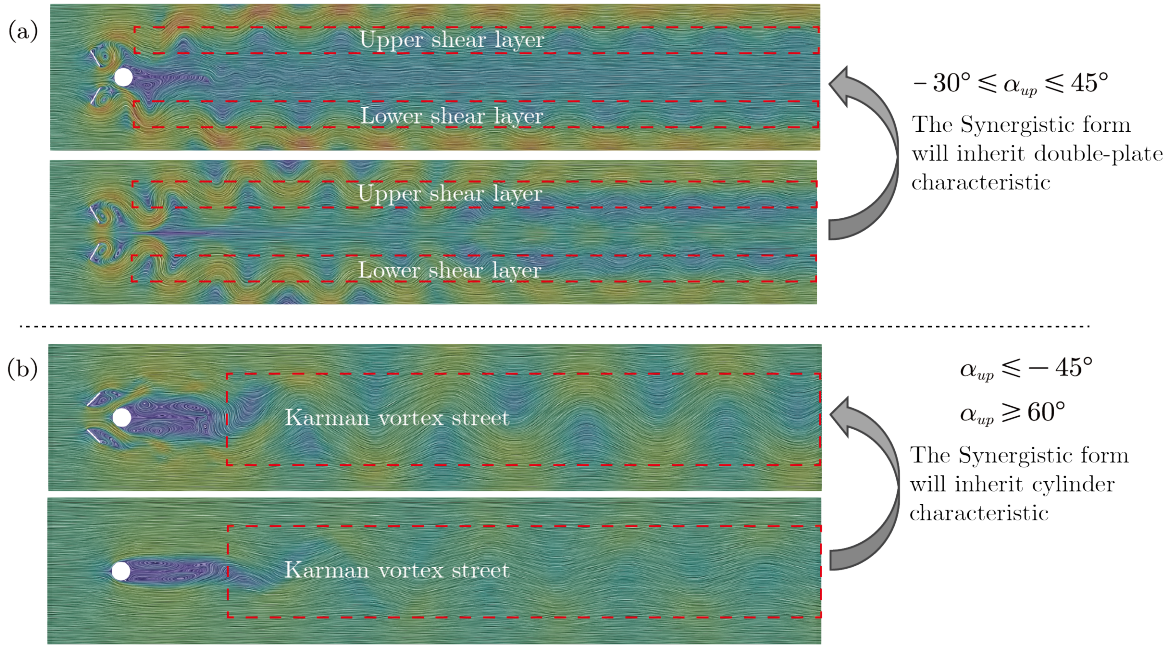

Figure 14: Schematic of the inheritance of wake characteristics from different vortex generators

amplitudes for the flag, which is similar to the scenario depicted in Figure 9, with vibration amplitudes of the same order of magnitude. However, there is a distinct phenomenon with the synergistic vortex generator compared to the double-plate-based vortex generator. When the inner vortexes v2 and v3 pass through the cylinder, they will be shifted to the positions even further outward than the vortexes v1 and v4. During this process, v2 and v3 may consume more energy, which makes their vortex intensities to be much weaker than v1 and v4.

In Figure 16, when $\alpha_{up} = -15°$, at time t_1, the two pairs of vortexes just start to shed along the edges of the double plates. Unlike in Figure 15 where at t_1 vortexes v2 and v3 (rotating in opposite directions) shed first, here v2 and v4 (rotating in the same direction) shed first instead. As they move downstream at different speeds, it will cause them to reach the flexible flag at different times. This results in alternating low-pressure zones acting on the upper and lower sides of the flag, creating a periodically varying lift force. The presence of the cylinder ensures that the vortexes remain stably alternating as they progress downstream, preventing a chaotic wake flow as seen in Figure 8, while maintaining the same vibration amplitudes. Specifically, similar to Figure 15, the cylinder here is acting more as a vortex path guider, yet its own vortex shedding is highly compressed and weaken. Hence the inner vortexes from double plates v2 and v3 move to the outer regions of the flow field compared to vortexes v1 and v4. Also it is can be seen that vortexes v1 and v4 play a dominant role in forming alternating low-pressure regions on the two sides of the piezoelectric flag. Vortexes v2 and v3, which dissipate rapidly, hardly influence the dominant vortexes v1 and v4, allowing v1 and v4 to stably exist in the wake field.

In Figure 17, with the plate angle at $\alpha_{up} = -45°$, the reduced block area of the plates allows significant vortex shedding behind the cylinder. At the same time, the cylinder still guides the inner vortexes v2 and v3 shed from the double plates to the outer fluid field. At time node t_3, vortexes v1 and v4, now in the inner wake side, have merged with other vortexes from the cylinder as they

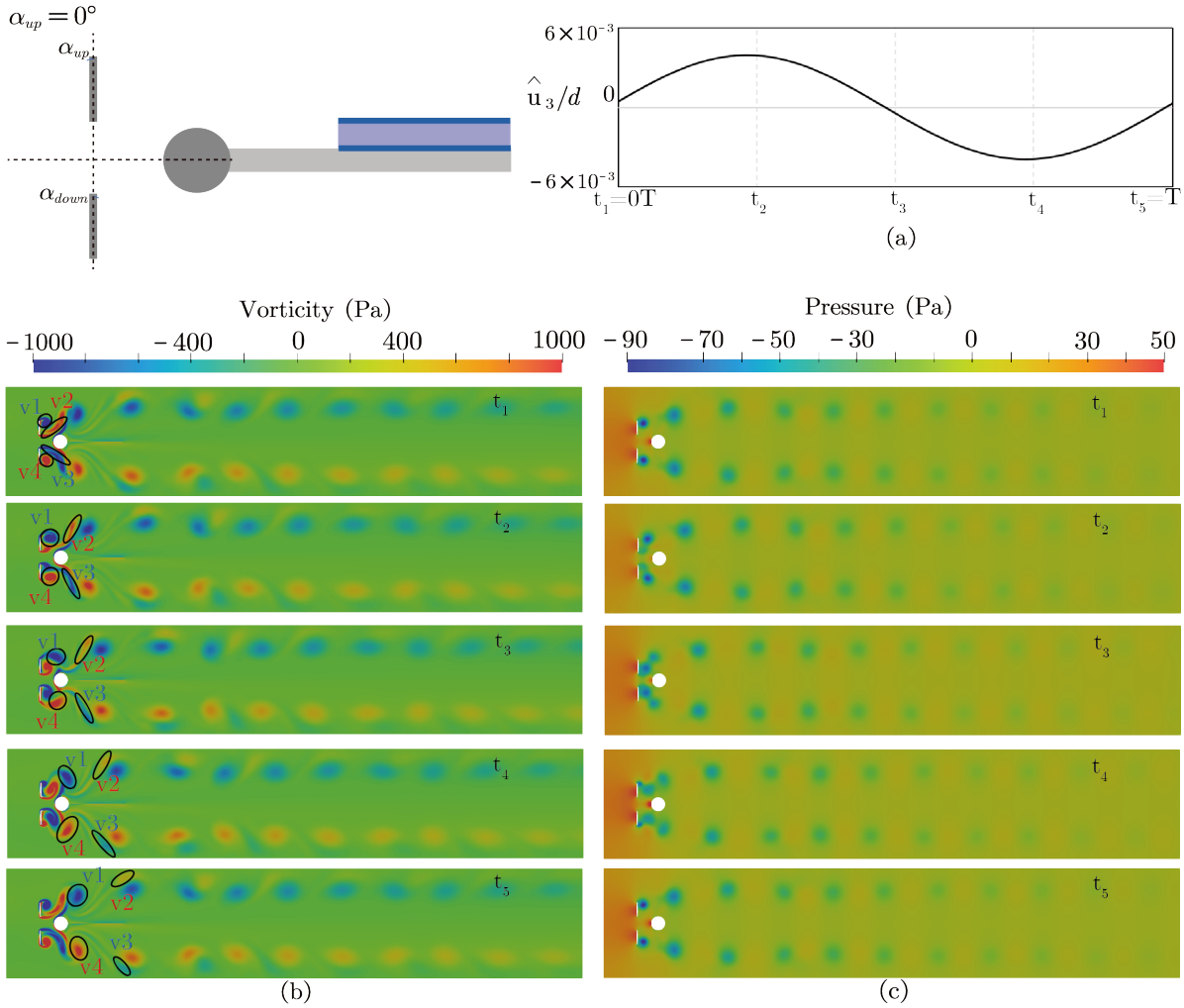

Figure 15: Flow field development process of synergistic energy harvester when $\alpha_{up} = 0°$.

develop downstream. The interaction and merging of vortexes in the current case contribute to a more complex and intense wake structure, leading to a larger pressure differential on the flag compared to the cylinder-based energy harvester, enhancing the vibration amplitude. We observe that the low-pressure regions in cylinder wake type cases are associated with the vortexes generated by the cylinder, which is very different from the double-plate wake type as shown in Figures 15 and 16. In these previous cases ($\alpha_{up} = 0°$ or $-15°$), the vortexes primarily originate from the double plates.

However, if the double-plate angle is too large, as in Figure 18 with $\alpha_{up} = 90°$, no alternating vortex shedding occurs behind the double plates. The synergistic energy harvester thus further changed to the cylinder-based energy harvester, resulting in smaller flag vibrations compared to those in Figure 17.

Figures 19 and 20 present the phase planes and full-body responses within vibration cycles for the synergistic energy harvester with different α_{up}. Compared to the double-plate-based energy harvester, the existence of the downstream rigid cylinder maintains the flexible flag's first mode shape and significantly enhances stability while sustaining a large amplitude. The system achieves a standard limit-cycle trajectory across various double plates angles. Although the case with $\alpha_{up} = 60°$ has weakest stability, but it is still more stable than the double-plate-based cases. When α_{up} is $-15°$ and $30°$, the phase

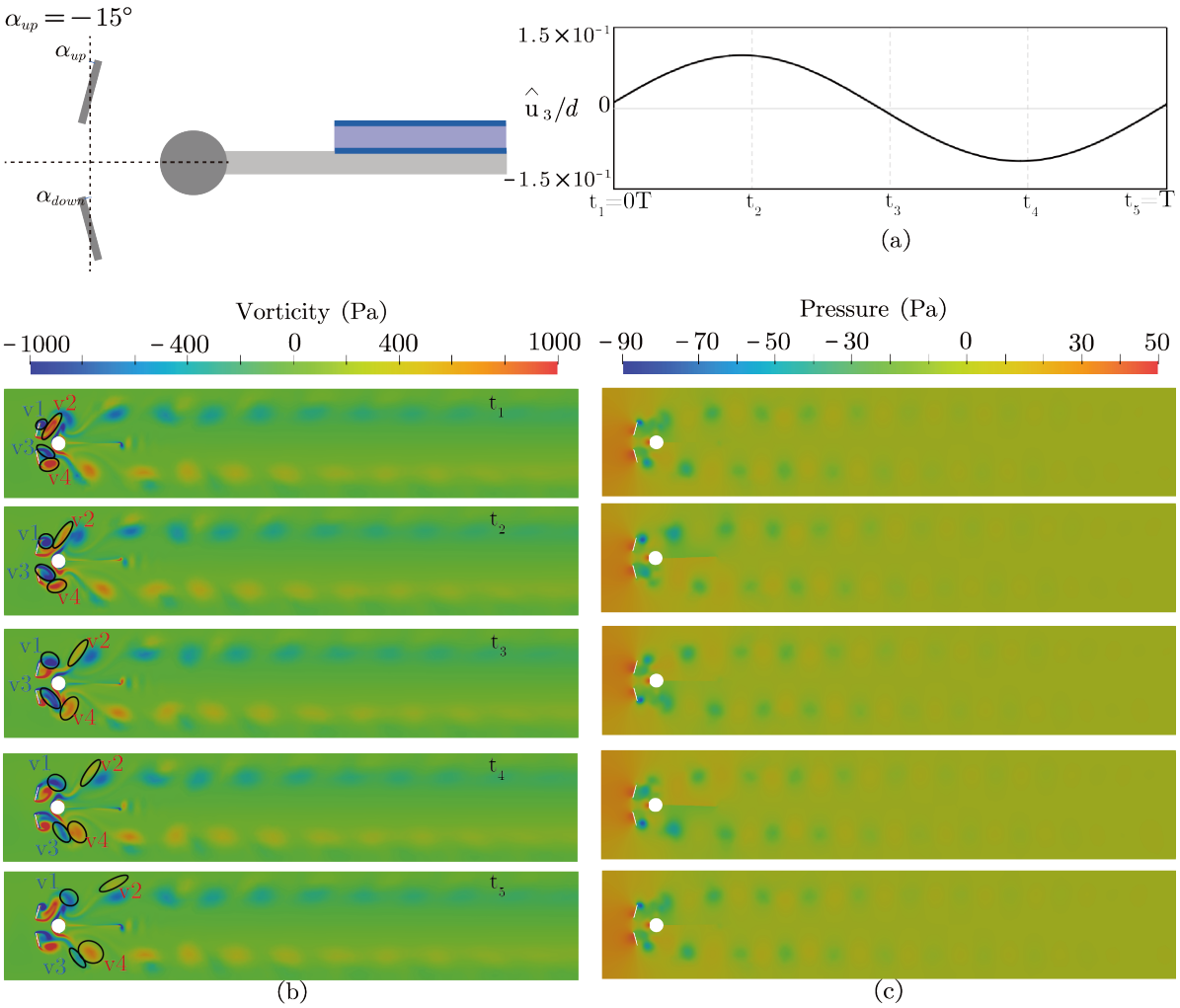

Figure 16: Flow field development process of synergistic energy harvester when $\alpha_{up} = -15°$.

planes are not only widest along the normalized displacement axis but also show a broader range along the normalized velocity axis, indicating they would have the higher oscillation frequency at these angles.

In Figure 21, the time domain results for the cylinder-based energy harvester, the double-plate-based energy harvester ($\alpha_{up} = -15°$), and the synergistic energy harvester ($\alpha_{up} = -15°$) are compared, including the displacement $\hat{u}_3$ at Point A, the potential output at Point B, and the lift force exerted by the fluid on the entire flexible flag. The synergistic energy harvester takes longer time to reach a periodic oscillation state. After the result of synergistic energy harvester ($\alpha_{up} = -15°$) become stable, it shows a 1.9 times higher vibration amplitude comparing to cylinder-based energy harvester. Also it will not exhibit the amplitude surges seen in the double-plate-based energy harvester while maintaining a higher oscillation frequency. This will result in a more stable and higher power output, which is favorable for energy harvesting.

Figure 22 presents the statistical results for the synergistic energy harvester at different upstream plate angles, with the dashed line representing the cylinder-based results. It can be observed that when the upstream plate angle $\alpha_{up} = -15°$ or 30°, forming asymmetric wakes with two shear layers, the flexible flag exhibits both high amplitude and frequency characteristics. This leads to a ten times

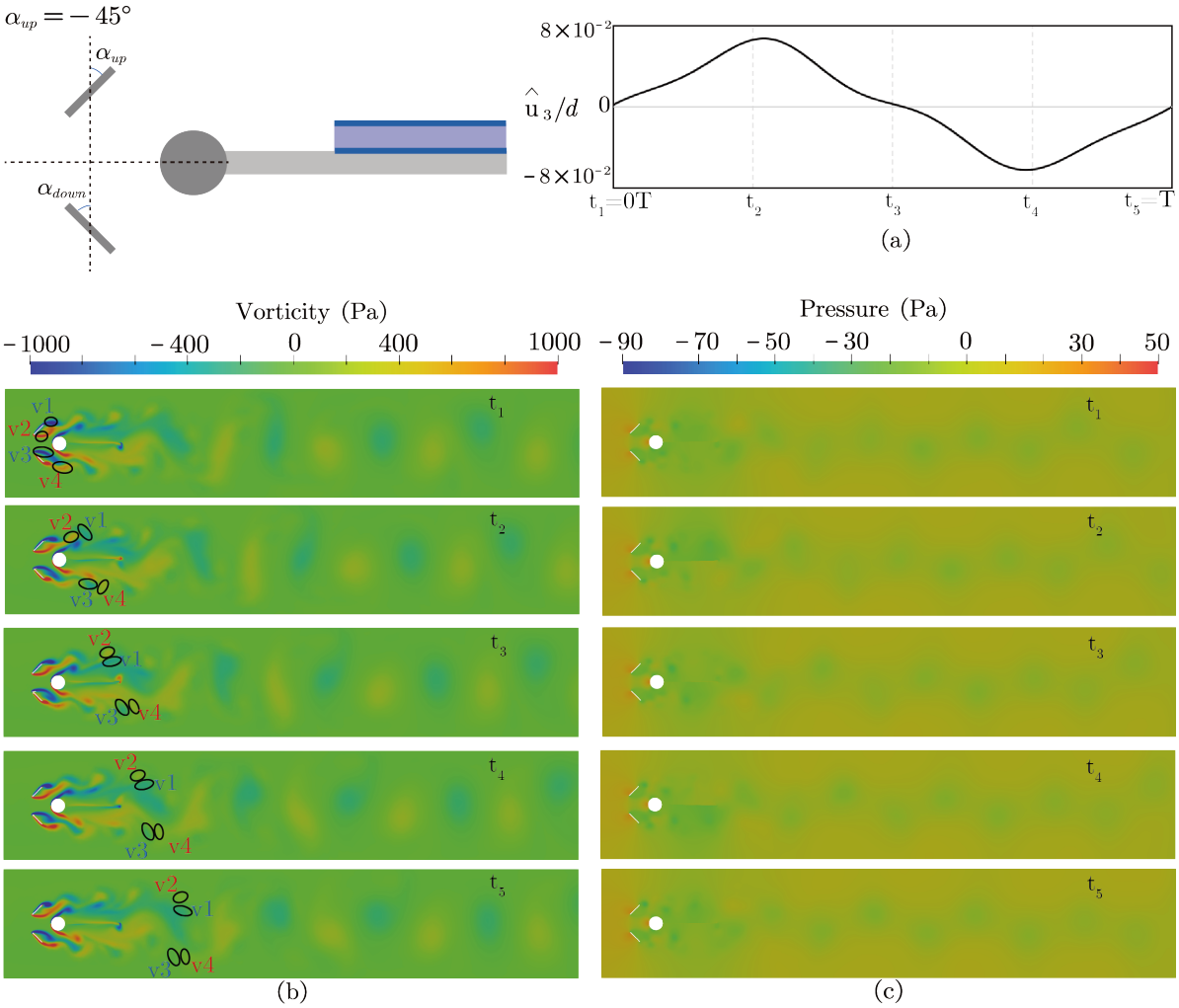

Figure 17: Flow field development process of synergistic energy harvester when $\alpha_{up} = -45°$.

increase in average power output compared to the cylinder-based energy harvester. It is well-known that high vibration amplitude typically results in higher power output. However, vibration frequency can also significantly enhance the energy harvester's electrical energy generation over a short period, as frequency is closely related to the flag's strain rate [39]. For the synergistic energy harvester, the flag's vibration is mainly influenced by the vortexes shed from the double plates with α_{up} in the range of $-30°$ to $45°$, and by the vortexes shed from the cylinder with α_{up} in the range of $-90°$ to $-45°$ and $60°$ to $90°$. Consequently, the vibration frequency with α_{up} in the range of $-30°$ to $45°$ is higher than at other angles, because the double plates and the cylinder shed vortexes at different frequencies. Then, according to the definition of energy harvesting efficiency, Efficiency $= \frac{\text{AveragedPower}}{0.5\rho\bar{v}^3(2\hat{u}_{3,\max})}$, if the increase in averaged power output is greater than the increase in $\hat{u}_{3,\max}$ while other factors remain constant, the efficiency of the energy harvester will be improved. Therefore, except for some angles that produce a symmetric wake, the efficiency of the synergistic energy harvester all get increased.

Apart from analyzing the energy harvesting performance of a single synergistic energy harvester, it is also important to observe its wake velocity distribution. This information is crucial for optimizing the layout when deploying multiple energy harvesters in a confined space as there will always be downstream

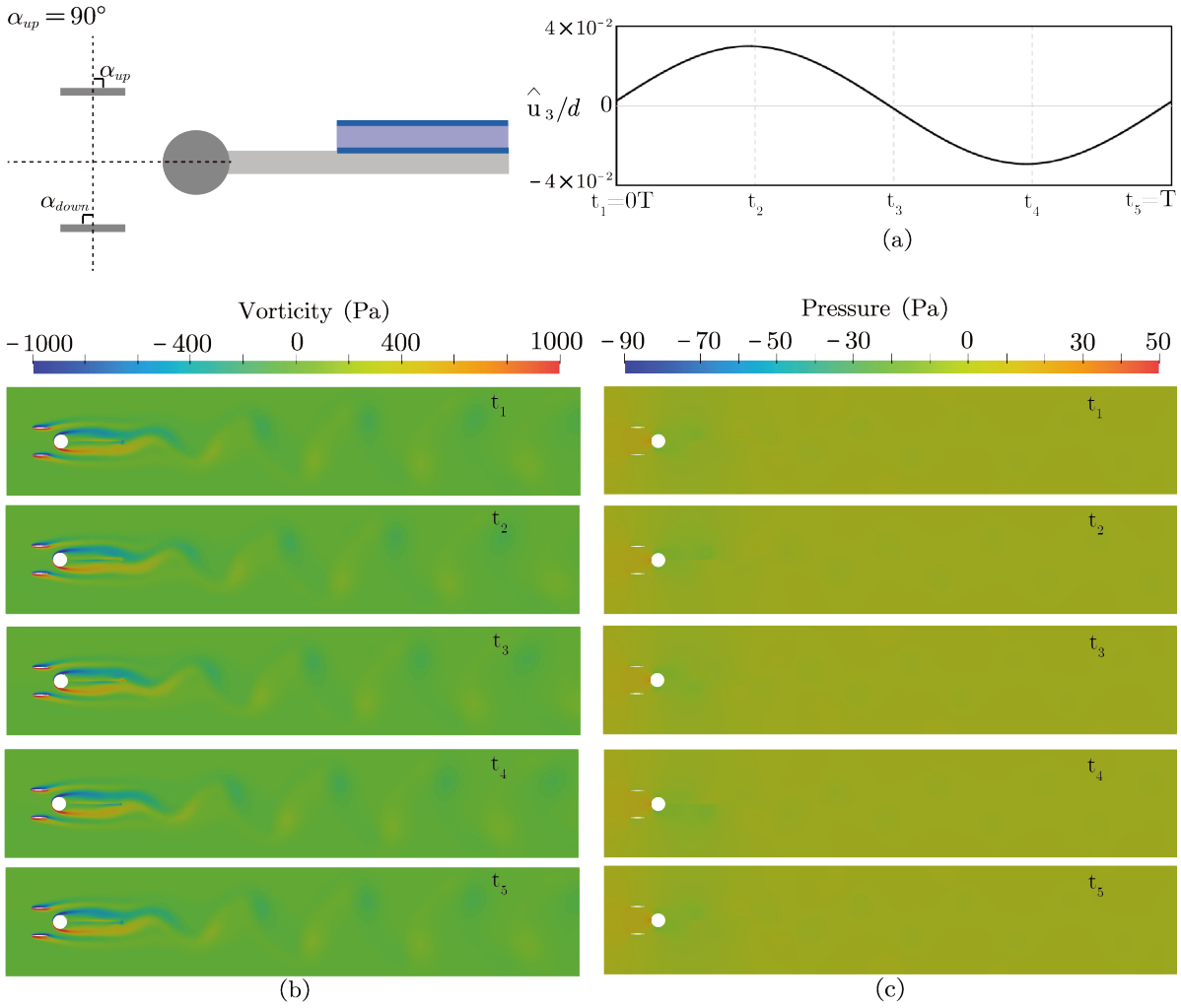

Figure 18: Flow field development process of synergistic energy harvester when $\alpha_{up} = 90°$.

harvesters placed inside the wake region of upstream harvesters. Therefore, in Figure 23, we present the velocity distribution along the centerline of the flow field for the synergistic energy harvester at different α_{up}. After a distance of $8d$ from the cylinder center, the wake velocity distributions show correlations with different wake types as described in Figure 13. Generally, the velocities in the cylinder wake type are higher than those in the double-plate wake type. This is because the double-plate wake type typically has two shear layers, between which a low-speed wake flow region forms. For this reason, when optimizing the arrangement of multiple energy harvesters, the synergistic energy harvester shows huge potential to be used to enhance the overall power output of multiple harvesters by adjusting the angle of the upstream double plates.

In summary, the synergistic energy harvester can achieve both the stability of the cylinder-based energy harvester and the large amplitude of the double-plate energy harvester by adjusting the angles of the double plates. Due to its stable, high-frequency, large-amplitude vibrations, the synergistic energy harvester significantly enhances both power output and efficiency. Additionally, the correlation between the angle of the upstream double plates and the wake velocity indicates that the synergistic energy harvester has great potential for application in the layout optimization of multiple energy harvesters.

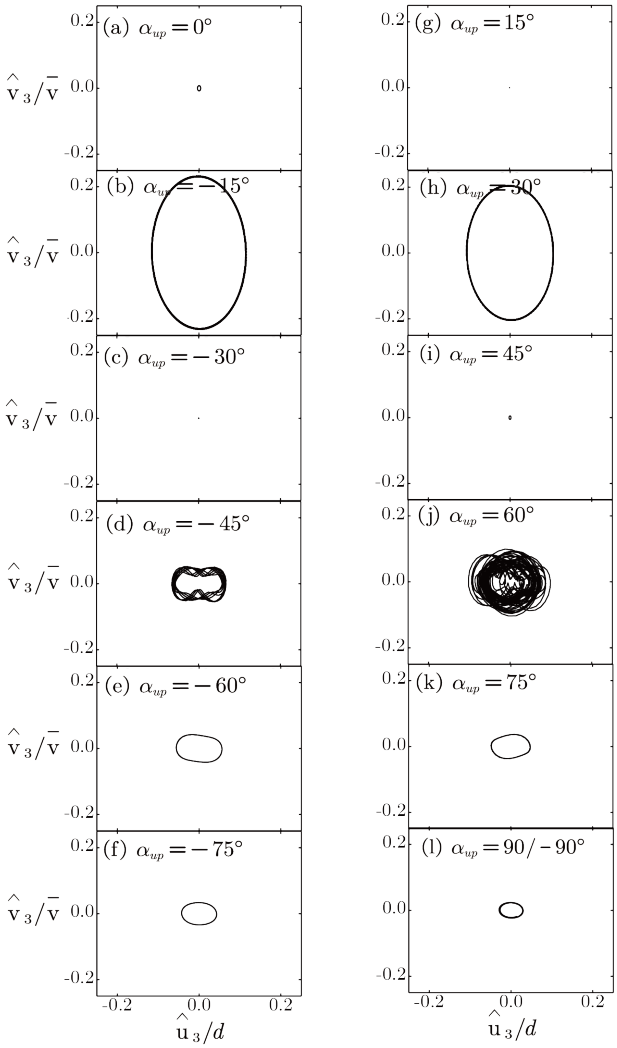

Figure 19: The phase plane trajectories for synergistic energy harvester with different α_{up}.

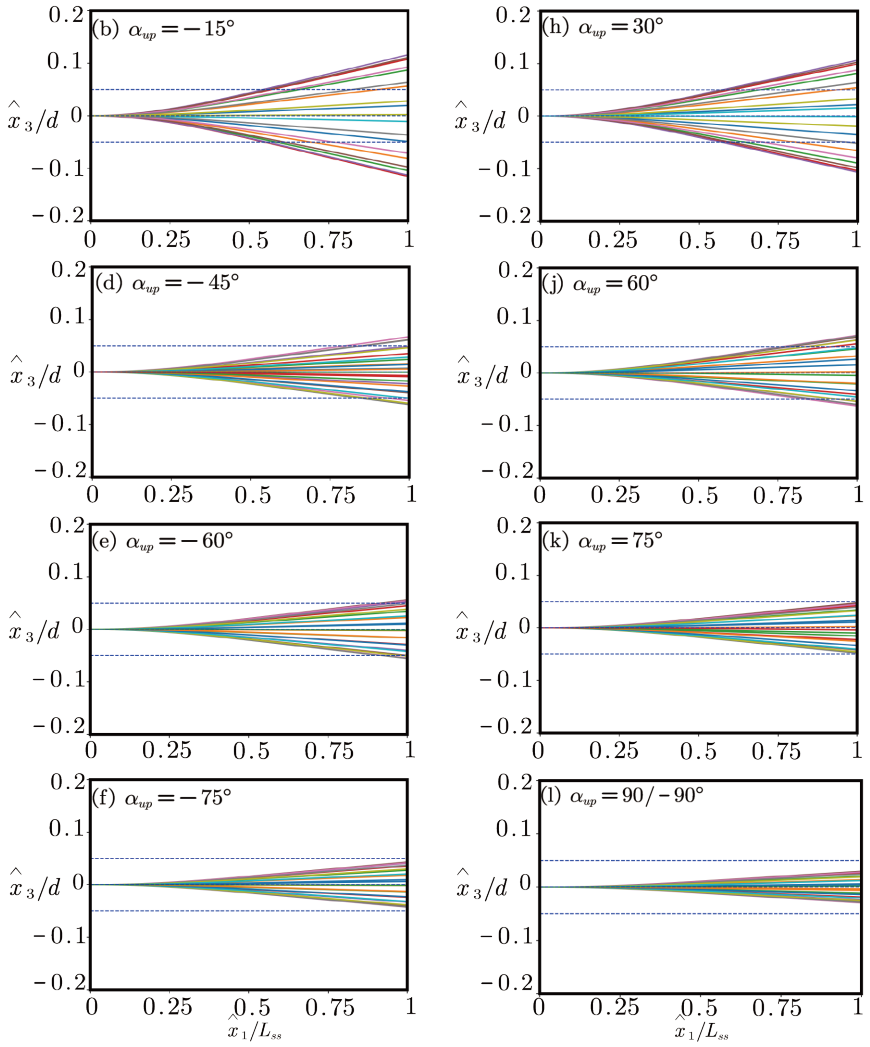

Figure 20: The full-body responses for synergistic energy harvester with different α_{up}.

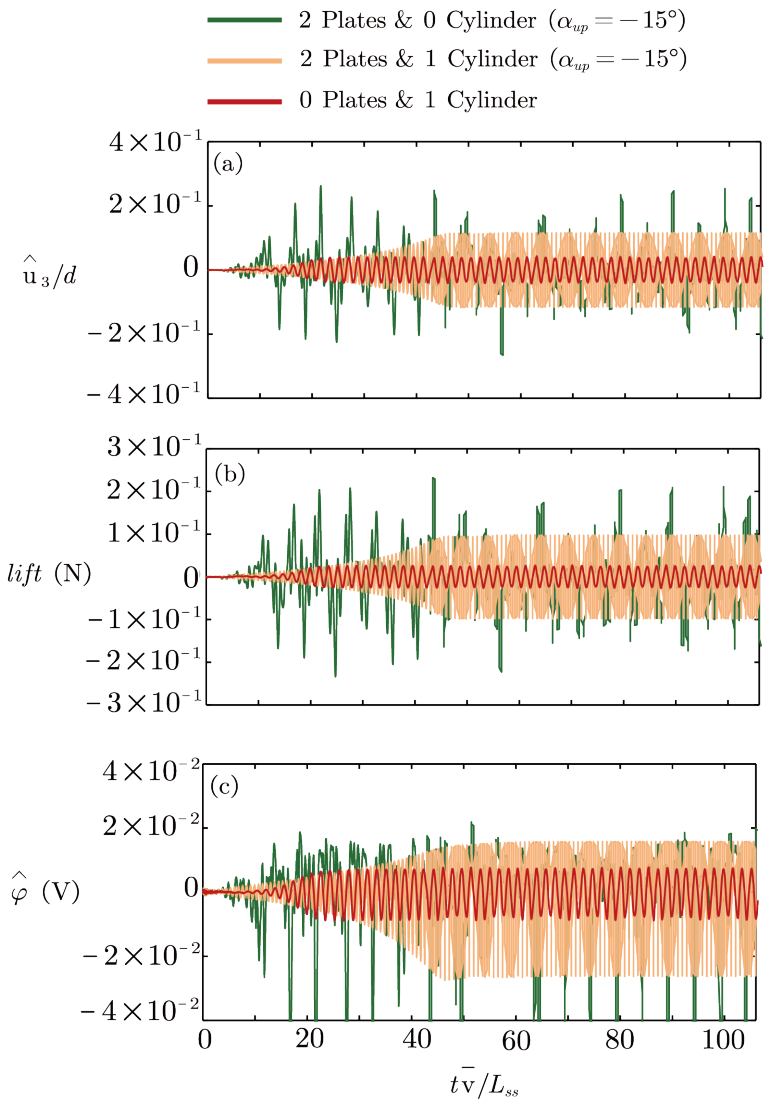

Figure 21: Time history of (a) displacement $\hat{u}_3$ of Point A in $\hat{x}_3$ direction, (b) lift force of the flag (without the rigid parts), (c) the potential $\hat{\phi}$ of Point B for cylinder-based energy harvester (1 Cylinder & 0 Plate) and double-plate-based energy harvester (0 Cylinder & 2 Plates $\alpha_{up} = -15°$) and synergistic energy harvester (1 Cylinder & 2 Plates $\alpha_{up} = -15°$).

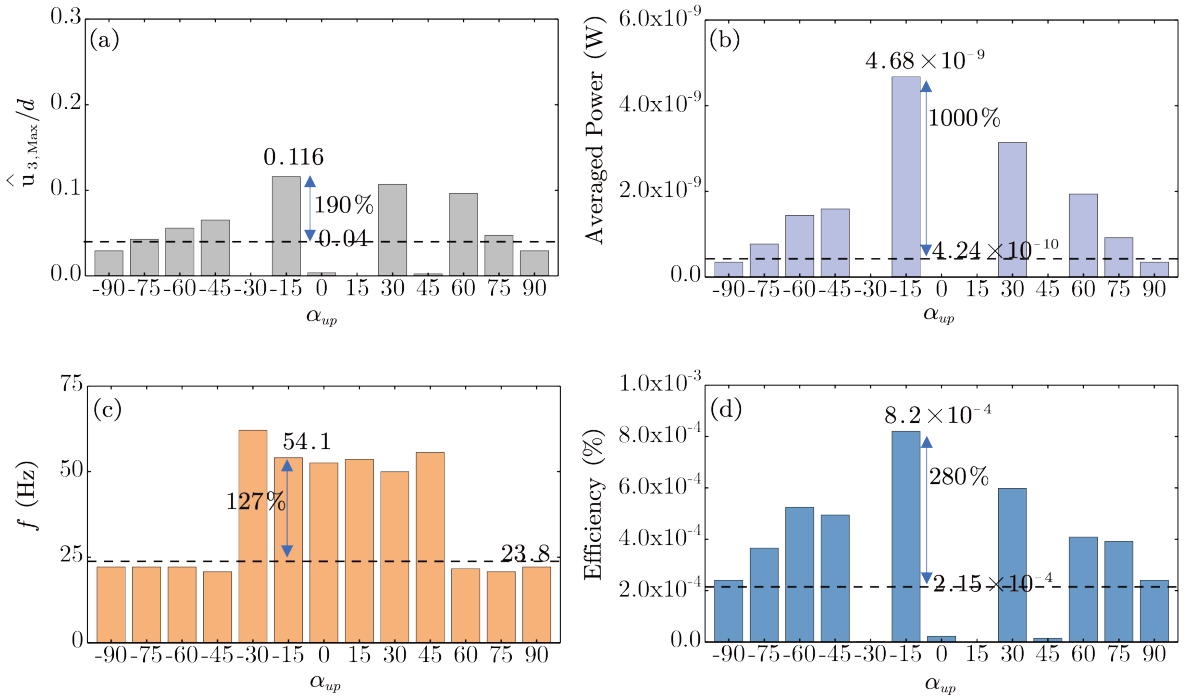

Figure 22: Statistic results of synergistic energy harvester with different α_{up}: (a) the maximum value of displacement $\widehat{u}_3$ of Point A in $\widehat{x}_3$ direction, (b) the averaged power, (c) the vibration frequency, (d) the energy harvesting efficiency.

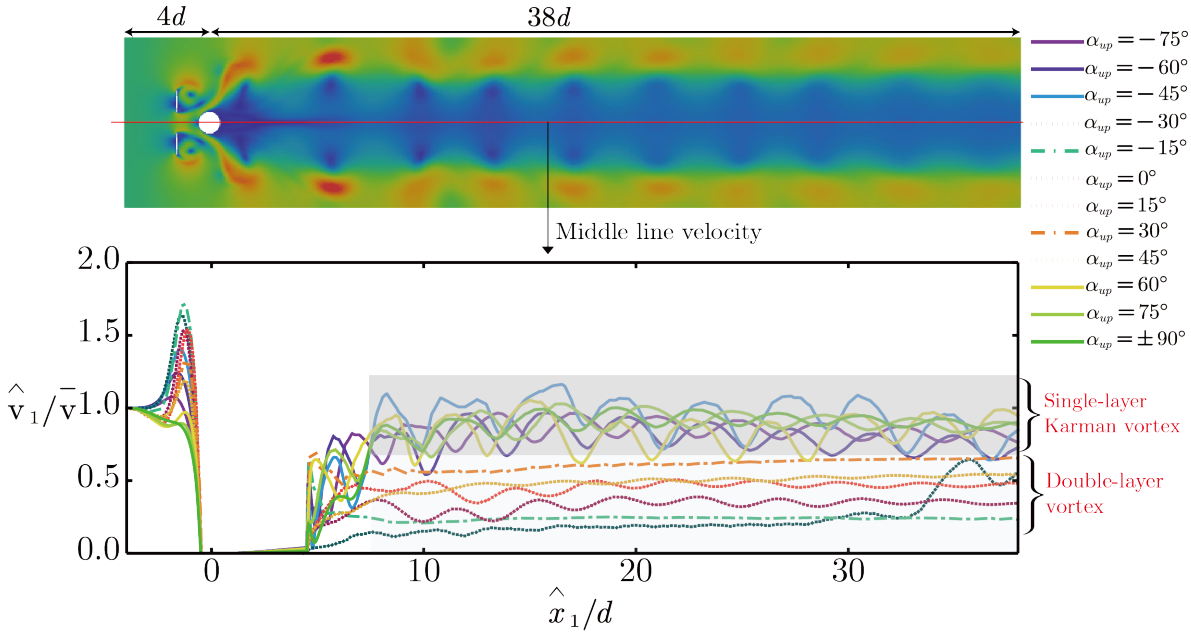

Figure 23: Velocity distribution along the center line of the flow field with synergistic energy harvester.

5 Conclusion

In this study, we numerically investigated the impact of a synergistic vortex generator, consisting of upstream side-by-side symmetric double plates and a downstream cylinder, on the vibration and energy harvesting performance of a head-fixed piezoelectric flag in a 2-D uniform laminar water flow. We focused on the different wake patterns formed by varying the angles of the double plates and analyzed their corresponding energy harvesting mechanisms and advantages.

Both the cylinder-based and double-plate-based energy harvesters can induce vibrations for the piezoelectric flag at relatively low water flow velocity, generating electrical energy. However, the cylinder-based harvester produces stable but small-amplitude vibrations, whereas the double-plate-based harvester produces larger amplitude vibrations but with lower frequency and poor stability. By using the synergistic harvester and adjusting the angle of the double plates, we can make use of the advantages of both separate vortex generators, achieving stable, high-frequency, and large-amplitude vibrations, thus obtaining greater and more stable power output. Specifically, at an angle of $-15°$, the synergistic harvester achieved an increase of 190% in vibration amplitude, 127% in vibration frequency, 1000% in average power output and 280% in energy harvesting efficiency compared to the classical cylinder-based harvester.

The synergistic vortex generator can form both double-plate and cylinder wake types by adjusting the double plate angles. In the double-plate wake type, the cylinder will guide the inner side vortexes from the double plates to the outer flow field, while the outer side vortexes shed from the double plates will stably influence and dominate the flexible flag vibration, by the alternating lift forces from the low-pressure vortexes. In the cylinder wake type, the vortex shedding intensity of the double plates decreases, and the vortexes shed by the cylinder dominate the flag vibrations. Still, the merging of vortexes from the double plates and the cylinder enhances the electrical output of the piezoelectric flag. Additionally, the center flow velocity in the cylinder-based wake is obviously higher than in the double-plate wake. This suggests that, adjusting the angle of the double plates might help achieve greater power output for the group harvesters in optimizing the layout of multiple synergistic harvesters.

This study is currently limited to low-velocity laminar flow environments. In the future, we plan to extend our research to high-velocity turbulent flow environments and explore different shapes of bluff bodies for further studies.

Acknowledgments

This work was supported by the China Scholarship Council (CSC No. 202106050012).

References

[1] J. Yick, B. Mukherjee, and D. Ghosal. Wireless sensor network survey. Computer Networks, 52(12):2292–2330, August 2008.

[2] B. Rashid and M. H. Rehmani. Applications of wireless sensor networks for urban areas: A survey. Journal of Network and Computer Applications, 60:192–219, January 2016.

[3] L. Shang, C. Hoareau, and A. Zilian. Optimal electrode coverage based on a new criterion for piezoelectric energy harvesters. Energy Conversion and Management, 284:116982, May 2023.

[4] O. Doaré and S. Michelin. Piezoelectric coupling in energy-harvesting fluttering flexible plates: linear stability analysis and conversion efficiency. Journal of Fluids and Structures, 27(8):1357–1375, November 2011.

[5] B. Zhang, B. Song, Z. Mao, W. Tian, and B. Li. Numerical investigation on viv energy harvesting of bluff bodies with different cross sections in tandem arrangement. Energy, 133:723–736, August 2017.

[6] R. Naseer and A. Abdelkefi. Nonlinear modeling and efficacy of viv-based energy harvesters: Monostable and bistable designs. Mechanical Systems and Signal Processing, 169:108775, April 2022.

[7] Y. Yang, L. Zhao, and L. Tang. Comparative study of tip cross-sections for efficient galloping energy harvesting. Applied Physics Letters, 102(6), February 2013.

[8] A. Abdelkefi, Z. Yan, and M. R. Hajj. Modeling and nonlinear analysis of piezoelectric energy harvesting from transverse galloping. Smart Materials and Structures, 22(2):025016, January 2013.

[9] R. Tang, Y. Gu, X. Mi, D. Yurchenko, F. Xu, W. Xu, X. Liu, and J. Wang. Numerical analysis of wiv phenomenon with two in-series cylinders: Wiv suppression and energy harvesting. Ocean Engineering, 262:112154, October 2022.

[10] M. Eugeni, H. Elahi, F. Fune, L. Lampani, F. Mastroddi, G. P. Romano, and P. Gaudenzi. Numerical and experimental investigation of piezoelectric energy harvester based on flag-flutter. Aerospace Science and Technology, 97:105634, February 2020.

[11] J. Dunnmon, S. Stanton, B. Mann, and E. Dowell. Power extraction from aeroelastic limit cycle oscillations. Journal of Fluids and Structures, 27(8):1182–1198, November 2011.

[12] M. Bryant, E. Wolff, and E. Garcia. Aeroelastic flutter energy harvester design: the sensitivity of the driving instability to system parameters. Smart Materials and Structures, 20(12):125017, November 2011.

[13] M. Zhang, C. Zhang, A. Abdelkefi, H. Yu, O. Gaidai, X. Qin, H. Zhu, and J. Wang. Piezoelectric energy harvesting from vortex-induced vibration of a circular cylinder: Effect of reynolds number. Ocean Engineering, 235:109378, September 2021.

[14] Navrose and S. Mittal. Lock-in in vortex-induced vibration. Journal of Fluid Mechanics, 794:565–594, April 2016.

[15] T. R. Sahu, M. Furquan, Y. Jaiswal, and S. Mittal. Flow-induced vibration of a circular cylinder with rigid splitter plate. Journal of Fluids and Structures, 89:244–256, August 2019.

[16] K. Yang, K. Su, J. Wang, J. Wang, K. Yin, and G. Litak. Piezoelectric wind energy harvesting subjected to the conjunction of vortex-induced vibration and galloping: comprehensive parametric study and optimization. Smart Materials and Structures, 29(7):075035, June 2020.

[17] J. Wang, S. Gu, C. Zhang, G. Hu, G. Chen, K. Yang, H. Li, Y. Lai, G. Litak, and D. Yurchenko. Hybrid wind energy scavenging by coupling vortex-induced vibrations and galloping. Energy Conversion and Management, 213:112835, June 2020.

[18] J. Wang, S. Zhou, Z. Zhang, and D. Yurchenko. High-performance piezoelectric wind energy harvester with y-shaped attachments. Energy Conversion and Management, 181:645–652, February 2019.

[19] U. Latif, C. Abdullah, E. Uddin, M. Y. Younis, M. Sajid, S. R. Shah, and A. Mubasha. Experimental and numerical investigation of the energy harvesting flexible flag in the wake of a bluff body. Wind and Structures, 26(5):279–292, 2018.

[20] D. Zhao, X. Hu, T. Tan, Z. Yan, and W. Zhang. Piezoelectric galloping energy harvesting enhanced by topological equivalent aerodynamic design. Energy Conversion and Management, 222:113260, October 2020.

[21] U. Latif, E. Uddin, M. Younis, J. Aslam, Z. Ali, M. Sajid, and A. Abdelkefi. Experimental electro-hydrodynamic investigation of flag-based energy harvesting in the wake of inverted c-shape cylinder. Energy, 215:119195, January 2021.

[22] A. Abdelkefi, J. M. Scanlon, E. McDowell, and M. R. Hajj. Performance enhancement of piezoelectric energy harvesters from wake galloping. Applied Physics Letters, 103(3), July 2013.

[23] G. R. S. ASSI, P. W. BEARMAN, and J. R. MENEGHINI. On the wake-induced vibration of tandem circular cylinders: the vortex interaction excitation mechanism. Journal of Fluid Mechanics, 661:365–401, August 2010.

[24] D. Zhao, J. Zhou, T. Tan, Z. Yan, W. Sun, J. Yin, and W. Zhang. Hydrokinetic piezoelectric energy harvesting by wake induced vibration. Energy, 220:119722, April 2021.

[25] M. Usman, A. Hanif, I.-H. Kim, and H.-J. Jung. Experimental validation of a novel piezoelectric energy harvesting system employing wake galloping phenomenon for a broad wind spectrum. Energy, 153:882–889, June 2018.

[26] R. Tang, Y. Gu, X. Mi, D. Yurchenko, F. Xu, W. Xu, X. Liu, and J. Wang. Numerical analysis of wiv phenomenon with two in-series cylinders: Wiv suppression and energy harvesting. Ocean Engineering, 262:112154, October 2022.

[27] J. Wang, L. Geng, M. Zhang, G. Zhao, M. Zhang, Z. Zhang, and Y. Li. Broadening band of wind speed for aeroelastic energy scavenging of a cylinder through buffeting in the wakes of a squared prism. Shock and Vibration, 2018:1–14, September 2018.

[28] L. Zhang, H. Dai, A. Abdelkefi, and L. Wang. Experimental investigation of aerodynamic energy harvester with different interference cylinder cross-sections. Energy, 167:970–981, January 2019.

[29] U. Latif, M. Y. Younis, S. Idrees, E. Uddin, A. Abdelkefi, A. Munir, and M. Zhao. Synergistic analysis of wake effect of two cylinders on energy harvesting characteristics of piezoelectric flag. Renewable and Sustainable Energy Reviews, 173:113114, March 2023.

[30] F.-R. Liu, W.-M. Zhang, L.-C. Zhao, H.-X. Zou, T. Tan, Z.-K. Peng, and G. Meng. Performance enhancement of wind energy harvester utilizing wake flow induced by double upstream flat-plates. Applied Energy, 257:114034, January 2020.

[31] F.-R. Liu, W.-M. Zhang, L.-C. Zhao, H.-X. Zou, T. Tan, Z.-K. Peng, and G. Meng. Performance enhancement of wind energy harvester utilizing wake flow induced by double upstream flat-plates. Applied Energy, 257:114034, January 2020.

[32] R. Zhang, Y. Cong, M. Sellam, A. Chpoun, and S. Gu. Advanced piezoelectric fluid energy harvesters by monolithic fluid-structure-piezoelectric coupling: A full-scale finite element model. Available at SSRN 4872878.

[33] B. T. Helenbrook. Mesh deformation using the biharmonic operator. International Journal for Numerical Methods in Engineering, 56(7):1007–1021, 2003.

[34] Automated Solution of Differential Equations by the Finite Element Method: The FEniCS Book. Springer Berlin Heidelberg, 2012.

[35] A. Bergersen, A. Slyngstad, S. Gjertsen, A. Souche, and K. Valen-Sendstad. turtlefsi: A robust and monolithic fenics-based fluid-structure interaction solver. Journal of Open Source Software, 5(50):2089, June 2020.

[36] H. Zhu, Q. Chen, T. Tang, M. M. Alam, T. Zhou, and J. Zhong. Flow-induced response and wake characteristics of a flexible splitter plate attached to a circular cylinder in laminar flow. Physics of Fluids, 35(12), December 2023.

[37] A. Erturk, P. A. Tarazaga, J. R. Farmer, and D. J. Inman. Effect of strain nodes and electrode configuration on piezoelectric energy harvesting from cantilevered beams. Journal of Vibration and Acoustics, 131(1), January 2009.

[38] S. Michelin and O. Doaré. Energy harvesting efficiency of piezoelectric flags in axial flows. Journal of Fluid Mechanics, 714:489–504, January 2013.

[39] U. Latif, M. Y. Younis, S. Idrees, E. Uddin, A. Abdelkefi, A. Munir, and M. Zhao. Synergistic analysis of wake effect of two cylinders on energy harvesting characteristics of piezoelectric flag. Renewable and Sustainable Energy Reviews, 173:113114, March 2023.